

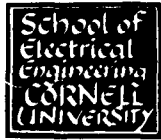
63-4-1

CATALOGED BY DDC

AS 1.2.10.

407 470

407 470



**CORNELL UNIVERSITY**

**SCHOOL OF ELECTRICAL ENGINEERING**

RESEARCH REPORT EE 546



# The Current Distributions in a Velocity-modulated Brillouin-focused Electron Beam

A. S. Gilmour, Jr.

L. F. Eastman

20 October 1962



LINEAR BEAM MICROWAVE TUBES, Technical Report No. 23

[Contract No. AF30(602)-2573]

School of Electrical Engineering  
CORNELL UNIVERSITY  
Ithaca, New York

RESEARCH REPORT EE 546

THE CURRENT DISTRIBUTIONS IN A VELOCITY-MODULATED  
BRILLOUIN-FOCUSED ELECTRON BEAM

A. S. Gilmour, Jr. and L. F. Eastman

LINEAR BEAM MICROWAVE TUBES

Technical Report No. 23

20 October 1962

Published under Air Force Contract No. AF30(612)-2573  
Rome Air Development Center, Griffiss Air Force Base, New York

## CONTENTS

	Page
ABSTRACT	v
I. INTRODUCTION	1
II. BRILLOUIN BEAM WITH SMALL-SIGNAL MODULATION	2
A. THEORY FOR IDEAL BRILLOUIN BEAM	2
1. Wave Propagation on Brillouin Beams	2
2. Velocity Modulation of Brillouin Beams	13
B. EXPERIMENTAL RESULTS WITH NONIDEAL BEAM	21
1. Approximations to Trapezoidal Beam	22
2. Comparison of Experimental Results with Approximations to Trapezoidal Beam	24
III. BRILLOUIN BEAM WITH LARGE-SIGNAL MODULATION	30
IV. CONCLUSIONS AND RECOMMENDATIONS	37
APPENDIX: PROBE CIRCUITRY FOR MEASURING R-F CURRENT	38
REFERENCES	49

## ABSTRACT

This report describes the radio-frequency current distributions in a Brillouin-focused electron beam that has been velocity-modulated by a gridless-gap cavity. The report gives a review of the small-signal theory of ideal Brillouin beams in addition to small- and large-signal experimental results. An approximation is made to predict the r-f current contours in a Brillouin beam whose d-c current-density profile resembles a trapezoid. The predictions of this theory are found to agree well with actual beam behavior in that both the thickness and the amplitude of the r-f current density ring around the beam vary with the depth of modulation  $a$  when  $a$  is very small. For values of  $a$  above 0.1, the amplitude of the current-density ring becomes constant while the thickness of the ring continues to vary.

The large-signal results show that an average nonlinear force is present, which causes the average diameter of the modulated beam to be smaller at some axial positions than the diameter of the d-c Brillouin beam. In addition, the large-signal results show that at least two second- and two third-harmonic waves are present on the beam. One of these in each case is the component arising from the square-wave current-density wave at the edges of the beam. The other wave in each case is thought to have arisen from the nonlinear drive in the high alternating fields in the cavity gap. Plasma-frequency reduction factors for these nonlinearly launched harmonic waves are found to agree extremely well with those computed from the small-signal theory.

## 1. INTRODUCTION

The work accomplished to date on the beam analyzer program at Cornell has dealt mainly with the characteristics of d-c Brillouin beams,<sup>1, 2</sup> and with the velocity distribution in the velocity-modulated Brillouin beam.<sup>3</sup> This work is very briefly reviewed in the Appendix. The purposes of this report are (1) to review the small-signal theory of the velocity modulation of ideal Brillouin beams, (2) to modify this theory for application to actual beams and compare its predictions with the small-signal r-f current contours found in the velocity-modulated beam described, and (3) to describe qualitatively the large-signal data obtained for fundamental and harmonic currents using the equipment described in the Appendix.

## II. BRILLOUIN BEAM WITH SMALL-SIGNAL MODULATION

### A. THEORY FOR IDEAL BRILLOUIN BEAM

In this section a general review is given of the small-signal theory of r-f disturbances on nonscalloping d-c Brillouin beams. Shown in Figure 1 is a sketch of the system to be analyzed. The review is divided into two main parts: The first is a description, originally presented by Rigrod and Lewis,<sup>4</sup> of the waves on a Brillouin beam; the second part deals with the modulation of a Brillouin beam by a gridless-gap cavity.

#### 1. Wave Propagation on Brillouin Beams

For an electron beam with no angular variation in charge density, fields, etc., the Lorentz force equation is

$$\ddot{r} - r\dot{\theta}^2 = -\eta(E_r + B_z r\dot{\theta}) \quad , \quad (1)$$

$$\frac{1}{r} \frac{d}{dt} (r^2 \dot{\theta}) = \eta B_z \dot{r} \quad , \quad (2)$$

$$\ddot{z} = -\eta E_z \quad , \quad (3)$$

where  $r$ ,  $\theta$ , and  $z$  are the co-ordinates of an electron in the beam. The d-c solutions to these equations, which are valid for nonscalloping Brillouin flow can be found in many references<sup>5, 6, 7</sup> and are

$$\begin{aligned} \dot{r} &= 0 \quad , \quad \dot{\theta} = \omega_L = \frac{\eta B_z}{2} \quad , \quad \dot{z} = u_0 \quad , \\ \eta E_r &= r\omega_L^2 \quad , \quad E_z = 0 \quad , \quad \rho_0 = \frac{2\epsilon_0 \omega_L^2}{\eta} \quad . \end{aligned} \quad (4)$$

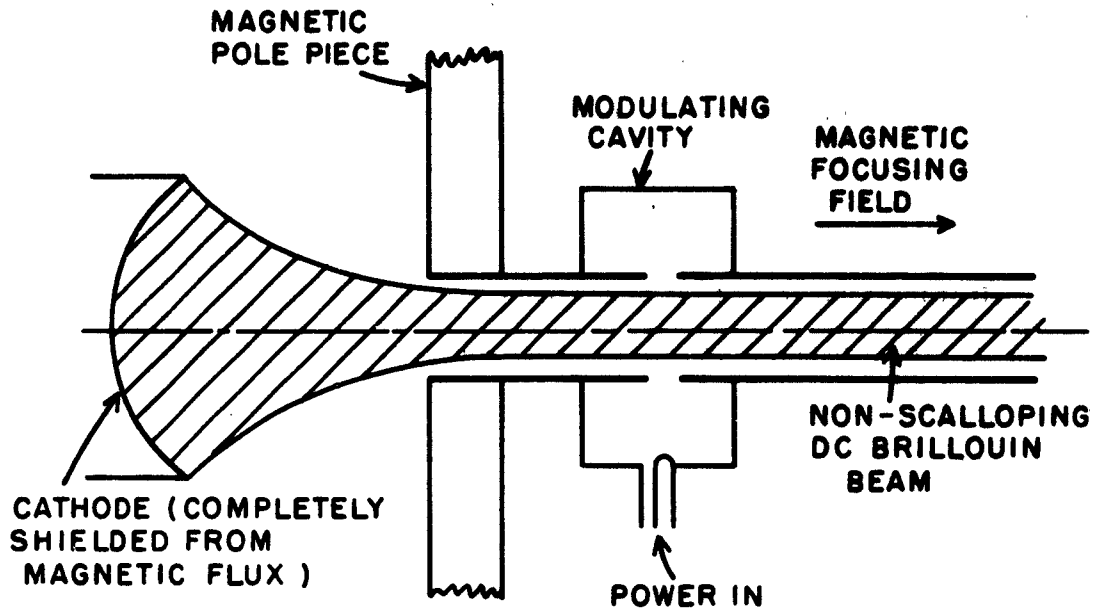


Figure 1. Diagram of Brillouin Beam and Modulating Cavity.

The important things to remember about the nonscalloping Brillouin beam are:

(1) that the axial velocity is constant throughout the beam even though effects of depression in potential are accounted for, and (2) that in practice, beams closely approximating Brillouin beams can be formed.<sup>1, 2</sup> It is expected, therefore, that measurements made on the nearly ideal beam should agree well with predictions of the behavior of a Brillouin beam.

If the initial positions of an electron in the Brillouin beam are designated as  $r_0$ ,  $\theta_0$ , and  $z_0$ , then at time  $t$ , the co-ordinate of the electron will be  $r_0$ ,  $\theta_0 + \omega_L t$ , and  $z_0 + u_0 t$ . When the Brillouin beam is velocity modulated at small-signal levels, these co-ordinates and the axial and radial electric fields are perturbed. For nonrelativistic velocities, effects that are due to a-c magnetic fields are small and may be neglected.

Since it is assumed that no flux is present in the cathode region, Equation (2) may be integrated to show that  $\dot{\theta} = \omega_L$ , even when r-f disturbances are present. Equation (1) may therefore be written as

$$\ddot{r} + r\omega_L^2 = -\eta E_r \quad (5)$$

If it is assumed that the perturbed co-ordinates and fields are written as  $r_o + r_1$  and  $E_{r_o} + E_{r_1}$ , where the subscript o identifies a d-c quantity and the subscript 1 identifies a r-f quantity; then Equation (5) may be written as

$$\ddot{r}_1 + (r_o + r_1)\omega_L^2 = -\eta(E_{r_o} + E_{r_1}) \quad (6)$$

and Equation (3) as

$$\ddot{z}_1 = -\eta E_{z_1} \quad (7)$$

It must be remembered that if the radial position of an electron in the beam varies, then the electron experiences a d-c electric field of magnitude,

$$-\eta E_{r_o} = \omega_L^2 (r_o + r_1) \quad (8)$$

Equation (8) is not valid for those electrons moving outside the outer diameter of the d-c Brillouin beam. This is because, as is shown in Figure 2, the radial electric field outside the beam is inversely proportional to radial position rather than directly proportional to it, as is the case inside the beam. If it is assumed that this error is small for small values of  $r_1$ , then Equation (6) becomes

$$\ddot{r}_1 = -\eta E_{r_1} \quad (9)$$



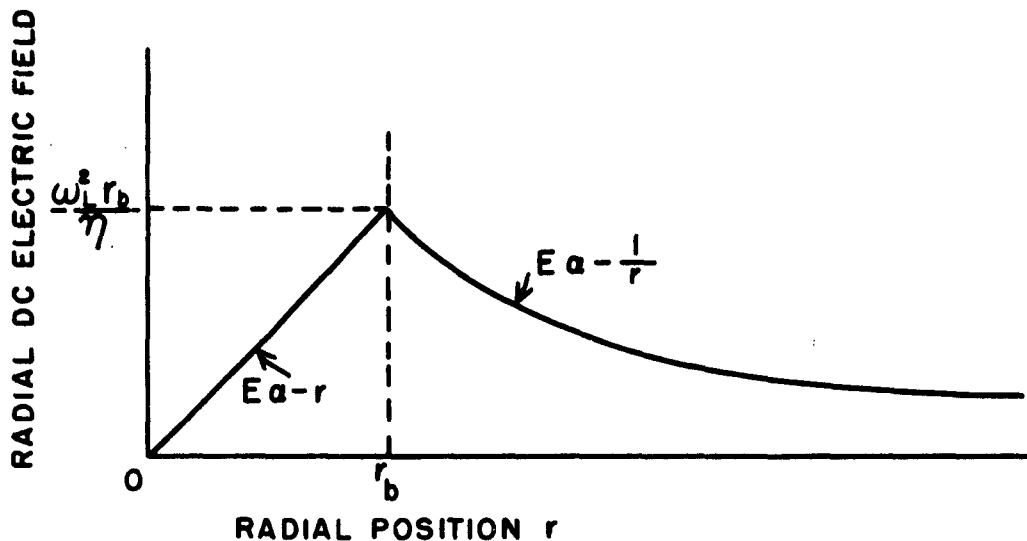


Figure 2. Radial Electric Field as Function of Radial Position for D-C Brillouin Beam ( $r_b$  = Outer Radius of D-C Brillouin Beam).

If it is assumed that all  $r$ -f quantities are small and that they vary as  $e^{j(\omega t - \gamma z)}$ , then

$$\frac{d}{dt} = j\omega_0(\beta_e - \gamma) \quad ,$$

where  $\beta_e = \frac{\omega}{u_0}$ , so that

$$\dot{r}_1 = j \frac{\eta}{u_0(\beta_e - \gamma)} E_{r1} \quad , \quad (10)$$

and

$$\dot{z}_1 = j \frac{\eta}{u_0(\beta_e - \gamma)} E_{z1} \quad . \quad (11)$$

The continuity equation may be written as

$$\nabla \cdot (\rho \underline{u}) = - \frac{\partial \rho}{\partial t}$$

or as

$$\rho_0 \underline{\nabla} \cdot \underline{u}_1 = - \frac{\partial \rho_1}{\partial t} - u_0 \frac{\partial}{\partial z} \rho_1 = - \frac{d}{dt} \rho_1 ; \quad (12)$$

so that

$$\rho_1 = j \frac{\rho_0}{u_0 (\beta_e - \gamma)} \underline{\nabla} \cdot \underline{u}_1 , \quad (13)$$

where

$$\underline{u}_1 = \underline{\dot{x}}_1 + \underline{\dot{z}}_1 .$$

Combining Equations (10), (11), and (13) gives the following equation for the r-f charge density:

$$\rho_1 = - \frac{\rho_0 \eta}{u_0^2 (\beta_e - \gamma)^2} \underline{\nabla} \cdot \underline{E}_1 = - \frac{\beta_p^2}{(\beta_e - \gamma)^2} \rho_1 , \quad (14)$$

since

$$\beta_p^2 = \frac{\omega_p^2}{u_0^2} = \frac{\eta \rho_0}{u_0^2 \epsilon_0} .$$

Equation (14) has two solutions:

$$\beta_p^2 = (\beta_e - \gamma)^2 , \quad (15)$$

and

$$\rho_1 = 0 . \quad (16)$$

Equation (15) leads to  $\gamma = \beta_e \pm \beta_p$ , which is the result found for infinite planar flow. This result cannot be accepted, since it is expected that the over-all behavior of a Brillouin beam should not differ appreciably from

the behavior of the beam with confined flow. That is, it is expected that  $\gamma = \beta_e \pm F\beta_p$ , where  $F$  is the plasma-frequency reduction factor; and that  $F \cong F_c$ , where  $F_c$  is the reduction factor for a beam with confined flow. Equation (16) states that the charge density within the modulated beam is  $\rho_0$ . This means, of course, that the r-f convection current must result mainly from changes in the beam radius, as is shown in Figure 3.

With the preceding information about the motion of electrons in the Brillouin beam, it is possible next to set up and solve the wave equations for the electric and magnetic fields in the beam. The reason for doing this is, of course, to determine the reduction factor  $F$  for the plasma oscillations in the beam. To facilitate the solving of the wave equations and to make the matching of boundary conditions simpler, it is convenient to make an approximation at the edge of the beam. This approximation in effect simply re-

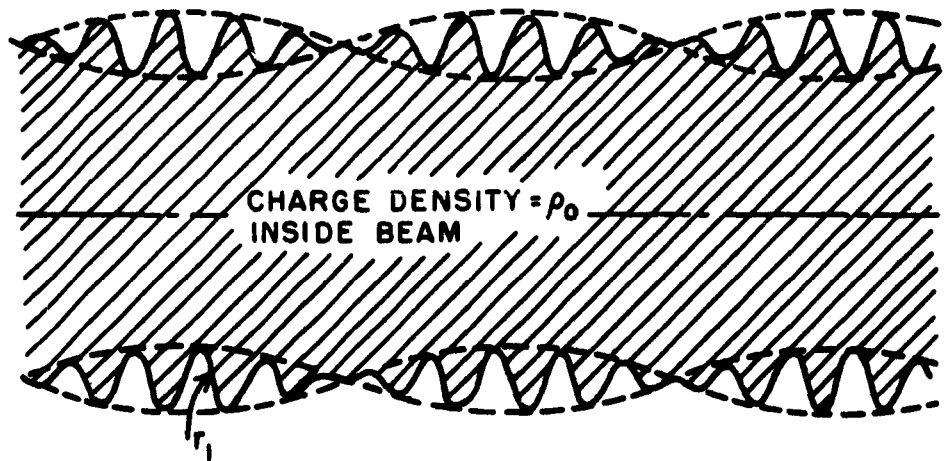


Figure 3. Diagram Showing R-F Modulation on Brillouin Beam. (Radius  $r_1$  varies as  $e^{j(\omega t - \gamma z)}$  where it is expected that  $\gamma = \beta_e \pm F\beta_p$ ).

places the rippling edge of the beam by the equivalent surface-current density,

$$G_z = \rho_0 r_1(r_0) u_0, \quad (17)$$

where  $r_1(r_0)$  is the value of the variable component of the radius evaluated at the d-c Brillouin beam radius. With this approximation, the beam may be considered to be a smooth cylinder surrounded by a shell of surface current.

From Maxwell's equations, now, the equations for the transverse-magnetic fields in the beam are found to be

$$\frac{1}{r} \frac{\partial}{\partial r} \left( r \frac{\partial E_{z1}}{\partial r} \right) - (\gamma^2 - k^2) E_{z1} = j\omega\mu J_{z1}, \quad (18)$$

$$\left( 1 - \frac{k^2}{\gamma^2} \right) E_{r1} = \frac{j}{\gamma} \frac{\partial E_{z1}}{\partial r} - j \frac{\omega\mu}{\gamma^2} J_{r1}, \quad (19)$$

and

$$H_{\theta 1} = \frac{j}{\gamma} J_{r1} + \frac{\omega\epsilon_0}{\gamma} E_{r1}, \quad (20)$$

where  $k^2 = \omega^2 \mu \epsilon_0$ . Since a nonrelativistic beam is being considered,  $k^2/\gamma^2 \ll 1$ . In addition  $J_z = \rho_0 \dot{z}_1$ , and  $J_r = \rho_0 \dot{r}_1$ , so from Equations (10) and (11), it is seen that

$$J_{z1} = j \frac{\epsilon_0 u_0 \beta^2}{(\beta_e - \gamma)} E_{z1}, \quad (21)$$

and

$$J_{r1} = j \frac{\epsilon_0 u_0 \beta^2}{(\beta_e - \gamma)} E_{r1}. \quad (22)$$

By substituting Equations (21) and (22) into Equations (18), (19), and (20) and by neglecting relativistic terms, one can obtain the following equations for the transverse-magnetic fields inside the beam:

$$\frac{1}{r} \frac{\partial}{\partial r} \left( r \frac{\partial E_{z_1}}{\partial r} \right) - \gamma^2 E_{z_1} = 0 \quad , \quad (23)$$

$$E_{r_1} = j \frac{\partial E_{z_1}}{\partial r} \quad , \quad (24)$$

$$H_{\theta_1} = \frac{\epsilon_o u_o}{\gamma} \left[ \beta_e - \frac{\beta_p^2}{(\beta_e - \gamma)} \right] E_{r_1} \quad . \quad (25)$$

Equation (23) (which is the same as the equation for the z-component of the electric field in a charge-free region), is as expected, since it was shown earlier that  $\rho_1 = 0$ . The solution to Equation (23) inside the beam must be  $E_{z_1} = A I_0(\gamma r)$ , since the electric field must be finite at  $R = 0$ . In the region outside the beam, where Equation (23) applies,

$$E_{z_1 \text{ out}} = B I_0(\gamma r) + C K_0(\gamma r) \quad . \quad (26)$$

The magnetic field inside the beam can be found from Equations (24) and (25) and is

$$H_{\theta_1} = j \frac{\epsilon_o u_o}{\gamma} \left[ \beta_e - \frac{\beta_p^2}{(\beta_e - \gamma)} \right] A I_1(\gamma r) \quad . \quad (27)$$

The magnetic field outside the beam is

$$H_{\theta_{1 \text{ out}}} = \frac{j\beta_e \epsilon_o u_o}{\gamma} [B I_1(\gamma r) - C K_1(\gamma r)] \quad (28)$$

In order to determine the constants A, B, and C, it is necessary to consider the boundary conditions at the drift-tube wall and at the edge of the beam. At the wall, where  $r = r_c$ , the z-directed electric field is zero, so

$$B = -C \frac{K_o(\gamma r_c)}{I_o(\gamma r_c)} \quad (29)$$

At the edge of the beam, the z-directed electric fields inside and outside of the beam must be equal, therefore

$$A I_o(\gamma r_b) = B [I_o(\gamma r_b) + C K_o(\gamma r_b)] \quad (30)$$

In addition, the magnetic field inside the beam plus the surface-current density at the edge of the beam must be equal to the magnetic field outside the beam. The surface-current density was  $G_z = \rho_o r_l(r_b) u_o$ , or with the aid of Equations (10) and (24),

$$G_z = j \frac{\beta_p^2 \epsilon_o u_o}{(\beta_e - \gamma)^2} A I_1(\gamma r_b) \quad (31)$$

Thus at the boundary where  $H_{\theta_1} - G_z = H_{\theta_{1 \text{ out}}}$ ,

$$\begin{aligned} j \frac{\epsilon_o u_o}{\gamma} \left[ \beta_e - \frac{\beta_p^2}{(\beta_e - \gamma)} \right] A I_1(\gamma r_b) - j \frac{\beta_p^2 \epsilon_o u_o}{(\beta_e - \gamma)^2} A I_1(\gamma r_b) \\ = \frac{j\beta_e \epsilon_o u_o}{\gamma} B [I_1(\gamma r_b) - C K_1(\gamma r_b)] \quad (32) \end{aligned}$$

Now, by eliminating the constants A, B, and C, one obtains the following equation:

$$\left(1 - \frac{1}{F_B^2}\right) \frac{I_1(\gamma r_b)}{I_0(\gamma r_b)} = \frac{I_1(\gamma r_b) + K_1(\gamma r_b) \frac{I_0(\gamma r_c)}{K_0(\gamma r_c)}}{I_0(\gamma r_b) - K_0(\gamma r_b) \frac{I_0(\gamma r_c)}{K_0(\gamma r_c)}}, \quad (33)$$

where  $F_B^2 = (\beta_e - \gamma)^2 / \beta_p^2$  is the reduction factor to be determined. By using the Wronskian relation,

$$I_0(\gamma r_b) K_1(\gamma r_b) + I_1(\gamma r_b) K_0(\gamma r_b) = \frac{1}{(\gamma r_b)},$$

one can rewrite

$$F_B^2 = \gamma r_b I_1(\gamma r_b) \left[ K_0(\gamma r_b) - \frac{I_0(\gamma r_b) K_0(\gamma r_c)}{I_0(\gamma r_c)} \right]. \quad (34)$$

Shown in Figure 4 are the plots of the plasma-frequency reduction factor  $F_B$  as a function of  $\gamma r_b$  for various ratios of the diameter of the drift tube to the beam diameter. It is interesting that the reduction factors are smaller than for confined-flow beams, and that the asymptotic value for  $F$  at large values of  $\gamma r_b$  is  $1/\sqrt{2}$  instead of unity, which is the value for the confined-flow beam. The reason for the low values of  $F$  is apparent when the fields at the edge of the beam are examined. As is shown in Figure 5, the axial r-f fields in the Brillouin beam are weakened by bulging both into and out of the beam. In the confined-flow beam, the axial fields near the edge of the beam are weakened by bulging outward, whereas the fields near the axis are only slightly weakened. Thus the net axial field causing plasma

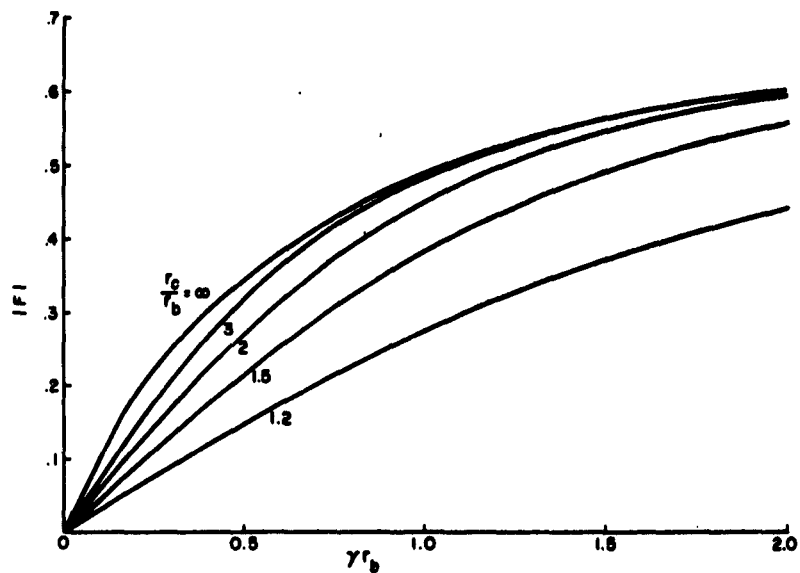


Figure 4. Plasma-Frequency Reduction Factors for Non-scalloping Brillouin Beams.

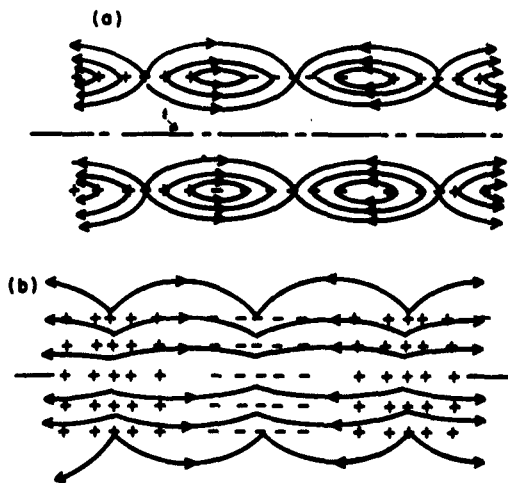


Figure 5. Diagram Showing Bulging of Electric Field Lines in (a) Brillouin Beam and (b) Confined Beam.



oscillations in the Brillouin beam is weaker than the one causing these oscillations in the confined beam, so that the reduction factor for the Brillouin beam is smaller than for the confined beam.

## 2. Velocity Modulation of Brillouin Beams

This part deals with the modulation of a Brillouin beam by a gridless-gap cavity and closely follows the work of Chodorow and Zitelli.<sup>8</sup> A sketch of a typical gridless-gap cavity and its orientation with respect to the beam is shown in Figure 1. Before computing the actual velocity modulation produced by the fields in the gap, we show that modulation by a gridless-gap cavity does launch the waves with zero r-f charge density, which were described in Section A1.

In the gap region, Equations (7) and (9) may be rewritten as

$$\ddot{r}_1 = -\eta(E_{r_1} + E_{c_r}) \quad , \quad (35)$$

and

$$\ddot{z}_1 = -\eta(E_{z_1} + E_{c_z}) \quad , \quad (36)$$

where  $E_{c_r}$  is the radial and  $E_{c_z}$  the axial component of the electric field produced by the cavity. Since Equations (35) and (36) are two components of a vector equation, and since under small-signal conditions, the operators  $d/dt$  and  $\nabla$  : are interchangeable, one obtains

$$\frac{d}{dt} \nabla \cdot \underline{u}_1 = -\eta \nabla \cdot (\underline{E}_{r_1} + \underline{E}_{z_1}) = \frac{\eta}{\epsilon_0} \rho_1 \quad . \quad (37)$$

But from Equation (12),

$$\rho_0 \nabla \cdot \underline{u}_1 = -\frac{d}{dt} \rho_1 \quad ; \quad (38)$$

therefore by combining Equations (37) and (38), one obtains

$$\frac{d^2}{dt^2} \rho_1 + \omega_p^2 \rho_1 = 0 . \quad (39)$$

Equation (39) states that a small volume of charge moving through the gap region must either vary in density as  $e^{j\omega_p z}$  or must not vary at all. Again,  $e^{j\omega_p z}$  variations must be rejected for the same reason that Equation (15) was rejected, and it is assumed that  $\rho_1 = 0$ .

If the gap dimensions are small compared to the free-space wavelength, the r-f electric fields in the gap region may be approximated by

$$E_{c_r} = j e^{j\omega t} \int_{-\infty}^{\infty} \frac{I_1(hr)}{I_0(hr_c)} A(h) e^{-jh z} dh , \quad (40)$$

and

$$E_{c_z} = e^{j\omega t} \int_{-\infty}^{\infty} \frac{I_0(hr)}{I_0(hr_c)} A(h) e^{-jh z} dh , \quad (41)$$

where  $h$  is a dummy variable of integration, and  $A(h)$  is a function to be determined by the boundary conditions at the drift-tube walls. A reasonable approximation to the field configuration at the drift-tube wall is that it is nearly the same as that between two knife edges; therefore

$$A(h) = \frac{V}{2\pi} J_0(hd/2) , \quad (42)$$

where  $V$  is the peak value of the gap voltage, and  $d$  is the distance between the gap edges.

The equation for the beam velocity in the gap,

$$\dot{\underline{u}}_1 = -\eta(\underline{E}_1 + \underline{E}_c) ,$$

can be written as

$$\frac{\partial}{\partial z} \underline{u}_1 + j\gamma \underline{u}_1 = -\frac{\eta}{u_0} \underline{E}_c , \quad (43)$$

where the effects of the electric fields originating from electron motions  $\underline{E}_1$  is approximated by changing  $j\beta_e$  to  $j\gamma$ ; therefore

$$\begin{aligned} \dot{\underline{r}}_1 &= -je^{j\omega t_0} \frac{\eta}{u_0} \int_{-\infty}^{\infty} e^{j\gamma z} \left\{ \int_{-\infty}^{\infty} \frac{A(h) I_1(hr)}{I_0(hr_b)} e^{-jh z} dh \right\} dz \\ &= ju_0 \frac{a}{2} \left[ J_0\left(\gamma \frac{d}{2}\right) \frac{I_1(\gamma r)}{I_0(\gamma r_c)} \right] e^{j\omega t_0} , \end{aligned} \quad (44)$$

and

$$\begin{aligned} \dot{\underline{z}}_1 &= -e^{j\omega t_0} \frac{\eta}{u_0} \int_{-\infty}^{\infty} e^{j\gamma z} \left\{ \int_{-\infty}^{\infty} \frac{A(h) I_0(hr)}{I_0(hr_c)} e^{-jh z} dh \right\} dz \\ &= u_0 \frac{a}{2} \left[ J_0\left(\gamma \frac{d}{2}\right) \frac{I_0(\gamma r)}{I_0(\gamma r_c)} \right] e^{j\omega t_0} , \end{aligned} \quad (45)$$

where, as usual,  $a$  is the depth of modulation and is equal to  $V/V_0$ . The time  $t_0$  is the time at which the electrons pass the position  $z = 0$  at the center of the gap. Now the velocities given by Equations (41) and (42), and the zero r-f charge density and zero radial displacement at  $z = 0$  are the

initial conditions for the waves described in Section A1. From Equations (10) and (11), and from the known variations of the electric fields with radius, it is seen that the magnitude of the radial and axial velocities after modulation can be written as

$$\dot{r}_1 = - \frac{\eta}{u_0(\beta_e - \gamma)} A I_1(\gamma r) ,$$

and

$$\dot{z}_1 = j \frac{\eta}{u_0(\beta_e - \gamma)} A I_0(\gamma r) ;$$

or as

$$\dot{r}_1 = j \left[ v_1 e^{-j\beta_q z} + v_2 e^{j\beta_q z} \right] I_1(\gamma r) e^{j(\omega t - \beta_e z)} , \quad (46)$$

and

$$\dot{z}_1 = \left[ v_1 e^{-j\beta_q z} + v_2 e^{j\beta_q z} \right] I_0(\gamma r) e^{j(\omega t - \beta_e z)} , \quad (47)$$

since both  $\dot{r}_1$  and  $\dot{z}_1$  vary as  $e^{j(\omega t - \gamma z)}$ , where  $\gamma = \beta_e \pm F\beta_p = \beta_e \pm \beta_q$ . At  $z = 0$ , Equations (46) and (47) can be equated to Equations (44) and (45), so that

$$v_1 + v_2 = u_0 \frac{a}{2} \frac{J_0\left(\gamma \frac{d}{2}\right)}{I_0(\gamma r_c)} . \quad (48)$$

Not only must the velocities in the drift tube and the gap be equal at  $z = 0$ , but the displacement of the electrons from their d-c positions must also be equal. In the drift tube, the radial displacement is

$$r_1 = - \frac{1}{\beta_q u_0} \left[ v_1 e^{-j\beta_q z} - v_2 e^{j\beta_q z} \right] I_1(\gamma r) e^{j(\omega t - \beta_e z)} \quad (49)$$

If it is assumed that no radial displacement of the electrons takes place in the gap, then at  $z = 0$ , one obtains  $r_1 = 0$ , and so  $v_1 = v_2$ . Finally, then, the equations for the electron velocities and for the  $r$ - $f$  component of the beam radius become

$$\dot{r}_1 = j u_0 \frac{a}{2} J_0\left(\gamma \frac{d}{2}\right) \frac{I_1(\gamma r)}{I_0(\gamma r_c)} \cos \beta_q z e^{j(\omega t - \beta_e z)} \quad (50)$$

$$\dot{z}_1 = u_0 \frac{a}{2} J_0\left(\gamma \frac{d}{2}\right) \frac{I_0(\gamma r)}{I_0(\gamma r_c)} \cos \beta_q z e^{j(\omega t - \beta_e z)} \quad (51)$$

and

$$r_1 = j \frac{1}{\beta_q} \frac{a}{2} J_0\left(\gamma \frac{d}{2}\right) \frac{I_1(\gamma r_b)}{I_0(\gamma r_c)} \sin \beta_q z e^{j(\omega t - \beta_e z)} \quad (52)$$

Equations (50), (51), and (52), and the condition that  $\rho_1 = 0$  show that there are two components of  $r$ - $f$  current density in the axial direction. The first, a volumetric current density, is simply the product  $\rho_0 \dot{z}_1$ . The second is a surface-current density that results from the rippling of the beam edge. If a Fourier analysis is made of the current density at  $r_b$ , which is the radius of the  $d$ - $c$  beam, it is evident that odd harmonics of current density are present, as well as the fundamental component, since the current density is a square wave. In fact, a complete expression for the surface current density is

$$J_z = J_0 \left( \frac{1}{2} - \frac{1}{\pi} \sin^{-1} \delta \right) + \frac{2J_0}{\pi} \sum_{n=\text{odd}}^{\infty} \frac{\cos(n \sin^{-1} \delta)}{n} \sin n\beta_e z$$

$$- \frac{2J_0}{\pi} \sum_{n=\text{even}}^{\infty} \frac{\sin(n \sin^{-1} \delta)}{n} \cos n\beta_e z \quad , \quad (53)$$

in which  $-1 \leq \delta \leq 1$  is a measure of the radial position  $r_\delta$ , at which  $J_z$  is to be evaluated and can be determined from

$$r_\delta = r_b + \delta A \sin \beta_q z \quad , \quad (54)$$

where

$$A = \frac{1}{\beta_q} \frac{a}{2} J_0 \left( \gamma \frac{d}{2} \right) \frac{I_1(\gamma r_b)}{I_0(\gamma r_c)} \quad . \quad (55)$$

Now, from Equation (53) and from  $\rho_0 z_1$ , the various components of the current in the modulated beam can be determined to be as shown in Figures 6 and 7. The curves in Figure 6 show the average, fundamental, 2nd-harmonic, and 3rd-harmonic current distributions as a function of the radial position in the beam for two drive levels. It is important to remember that the integral across the beam of any harmonic-current component vanishes. For the second harmonic component, for example, the current peak inside  $r_b$  is  $180^\circ$  out of phase with the current peak outside  $r_b$ , so that the net second-harmonic current is zero. Thus, only the fundamental current component can induce currents in an external circuit. The curves in Figure 7 show the average and fundamental currents as functions of the horizontal

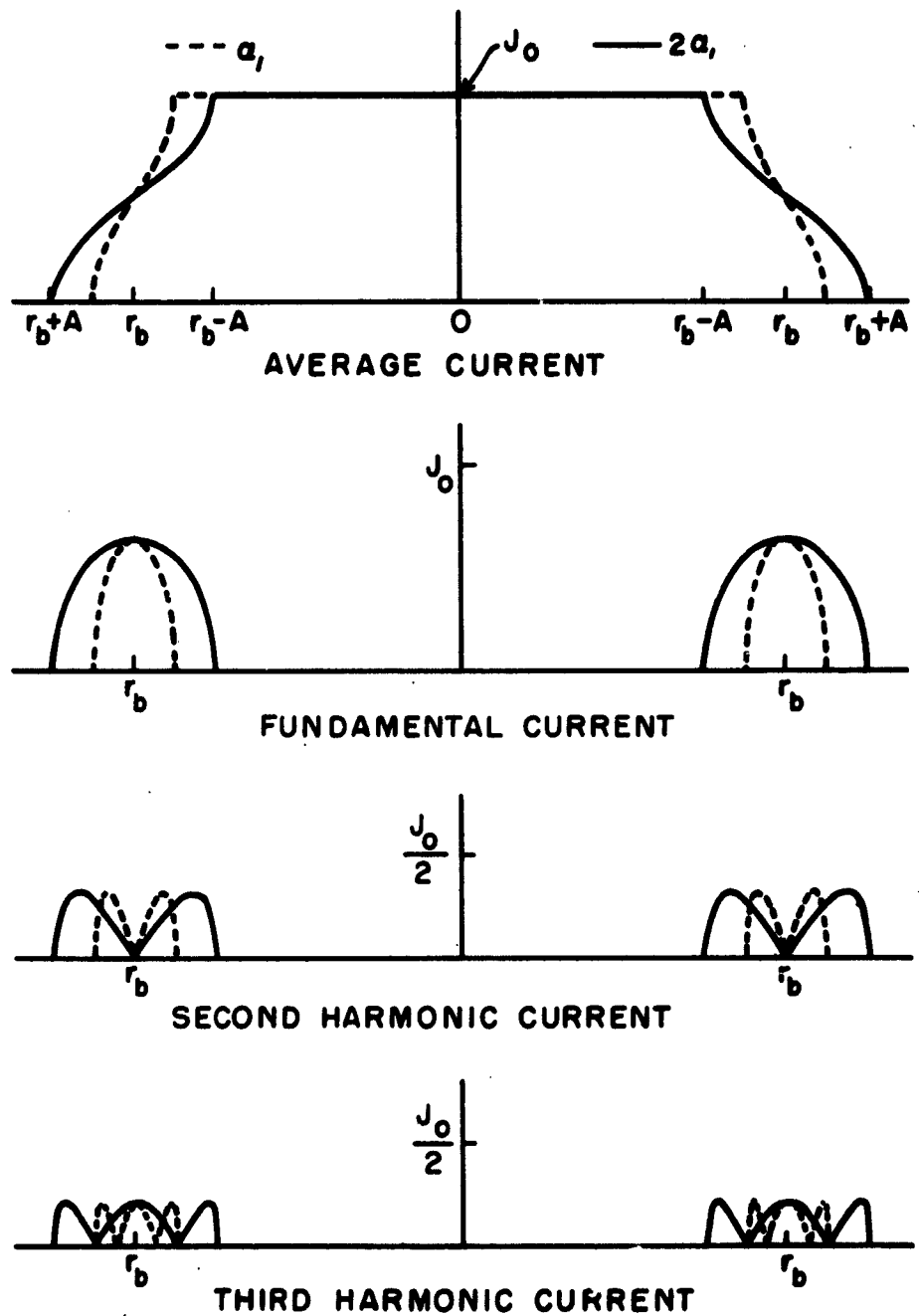


Figure 6. Components of Current in Brillouin Beam, Velocity-modulated at Small-Signal Levels.

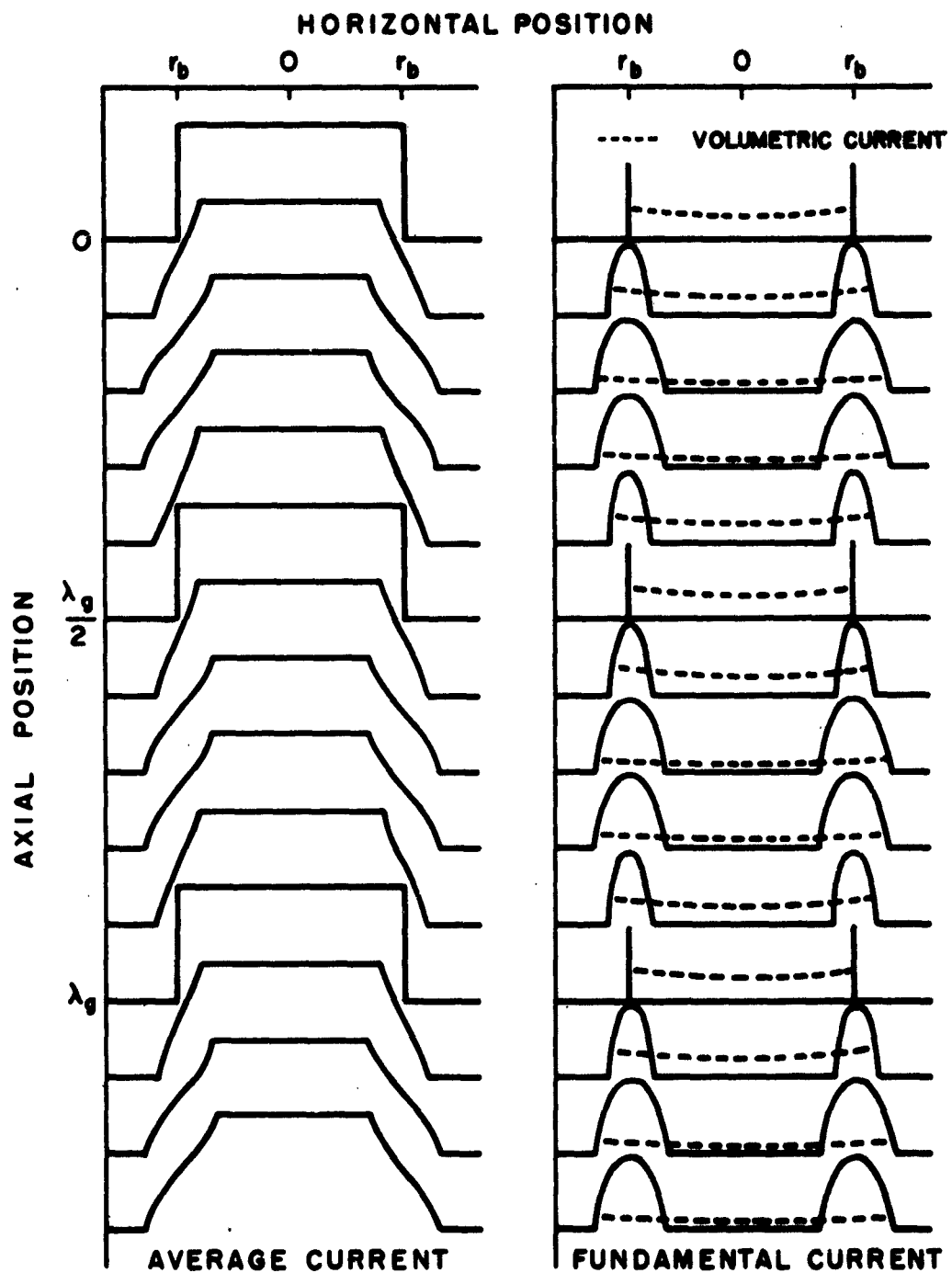


Figure 7. Average and Fundamental Currents as Functions of Horizontal and Axial Positions.



and axial positions in the beam. The zero position is where the modulating cavity is assumed to be. Note that exaggerated curves in the volumetric current are included in the plot of fundamental current. Note also that the volumetric current goes to zero at horizontal positions that are  $\lambda_q/4$  from the zeros of the surface current.

The magnitude of the volumetric current in the beam is simply the integral of  $\rho_o \dot{z}_1$  across the beam and is therefore

$$I_v = \int_0^{r_b} \rho_o \dot{z}_1 2\pi r dr \quad ,$$

or

$$I_v = \frac{2\pi r_b J_o}{\gamma} \frac{a}{2} J_o \left( \gamma \frac{d}{2} \right) \frac{I_1(\gamma r_b)}{I_o(\gamma r_c)} \cos \beta_q z e^{j(\omega t - \beta_e z)} \quad (56)$$

The surface current is  $2\pi r_b \rho_o u_o r_1$ ; therefore

$$I_s = j \frac{2\pi r_b J_o}{\beta_q} \frac{a}{2} J_o \left( \gamma \frac{d}{2} \right) \frac{I_1(\gamma r_b)}{I_o(\gamma r_c)} \sin \beta_q z e^{j(\omega t - \beta_e z)} \quad (57)$$

The ratio of the maximum value of  $I_v$  to the maximum value of  $I_s$  is therefore seen to be  $\beta_q/\gamma$ ; therefore the volumetric current can normally be neglected.

## B. EXPERIMENTAL RESULTS WITH NONIDEAL BEAM

This section consists of two parts. The first presents modification of the ideal beam theory, which takes into account the fact that the curve of charge density as a function of radius in actual beams is more nearly

trapezoidal than rectangular in shape, as shown in Figure 8. (This distortion of the ideal beam is due mainly to the thermal velocities of the electrons.) The second part of this section presents a comparison of the predictions of the first part with data taken on a nearly ideal Brillouin beam. A very brief description of this beam and of the equipment used to obtain it is given in the Appendix. More complete descriptions are included in reports by Gilmour<sup>1, 3</sup> and Hallock<sup>2</sup>.

#### 1. Approximations to Trapezoidal Beam

Since the part of the d-c trapezoidal beam where the charge density is constant behaves like a Brillouin beam, it can be assumed that there is no r-f space-charge density. This means, of course, that when the beam tends to bunch in the axial direction, an expansion in the radial direction occurs, which is sufficient to prevent bunching. Under small-signal conditions, if the distance in which the charge density drops from  $\rho_0$  to zero is small compared to the radius  $r_b$ , it may be assumed that the radial excursion of all parts of the sloping beam edge is the value of  $r_1(b)$  given in Equation (52) for the beam with vertical edges. Therefore, as is shown in Figure 9, when the depth of modulation  $a$  is very small, the r-f current density waveform at  $r(b)$  is a sinusoid. For the beam with vertical edges, it was shown that this waveform is a square wave. As  $a$  is increased, the excursions of the beam edge become large enough to cause the peaks of the sine wave to become clipped. Finally for a reasonably large  $a$ , the current density waveform closely approximates a square wave.

Shown in Figure 10 are curves of the fundamental current density as a function of radius for various drive levels. Notice that for small drive



Figure 8. Charge Density as a Function of Radial Position for (a) Ideal Beam, (b) Practical Beam.

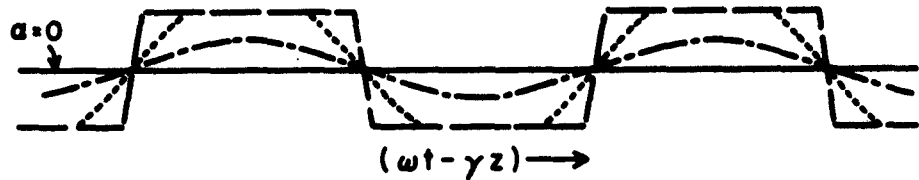


Figure 9. R-F Current Density Waveform at  $r(b)$  as a Function of  $(\omega t - \gamma z)$  for Various Drive Levels.

KEY FOR  
FIGS. 9  
AND 10

————	LARGE $\alpha$
-----	MEDIUM $\alpha$
- · - · -	SMALL $\alpha$

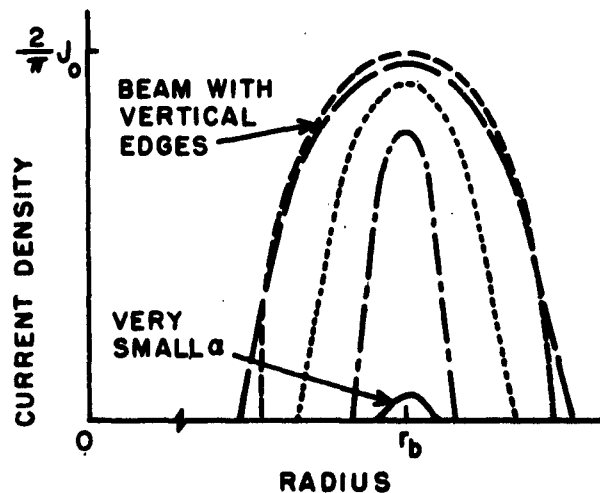


Figure 10. Curves of Fundamental Current Density as a Function of Radius for Various Drive Levels.

levels, both the amplitude and the width of the current profile change; whereas at large signal levels, the amplitude is nearly constant, but the width of the profile changes. For the beam with vertical edges, it should be remembered that the amplitude of the current-density profile is always  $\frac{2}{\pi} J_0$  and that only the width of the profile changes with  $a$ . Approximate curves of the average and fundamental current densities as functions of the horizontal and axial positions in the beam for a reasonably large value of  $a$  (still within the small-signal range) are shown in Figure 11.

No mention has been made yet of the harmonic current densities generated by small-signal modulation of the trapezoidal beam. It was shown in Figure 9 that at the radial position  $r(b)$ , no harmonic signals are generated as long as the  $a$  is small enough to prevent clipping of the sinusoid. Harmonics are still generated at radii greater and smaller than  $r(b)$ , where clipping of the sinusoid does take place, but, these are much smaller than those generated in the case of the beam with vertical edges. How much the harmonic amplitude in the trapezoidal beam decreases depends, of course, upon the slope of the edge of the beam.

## 2. Comparison of Experimental Results with Approximations to Trapezoidal Beam

Shown in Figure 12 are plots of the average and fundamental currents taken at a small-signal level with the apparatus described in the Appendix and elsewhere<sup>1, 2, 3</sup>. The current data are plotted as a function of the horizontal position for various axial positions along the beam. Notice that the average current profiles indicate that this beam closely approximates the trapezoidal beam described in the previous section. The drive level in Figure 12 is low enough so that the difference between the average current

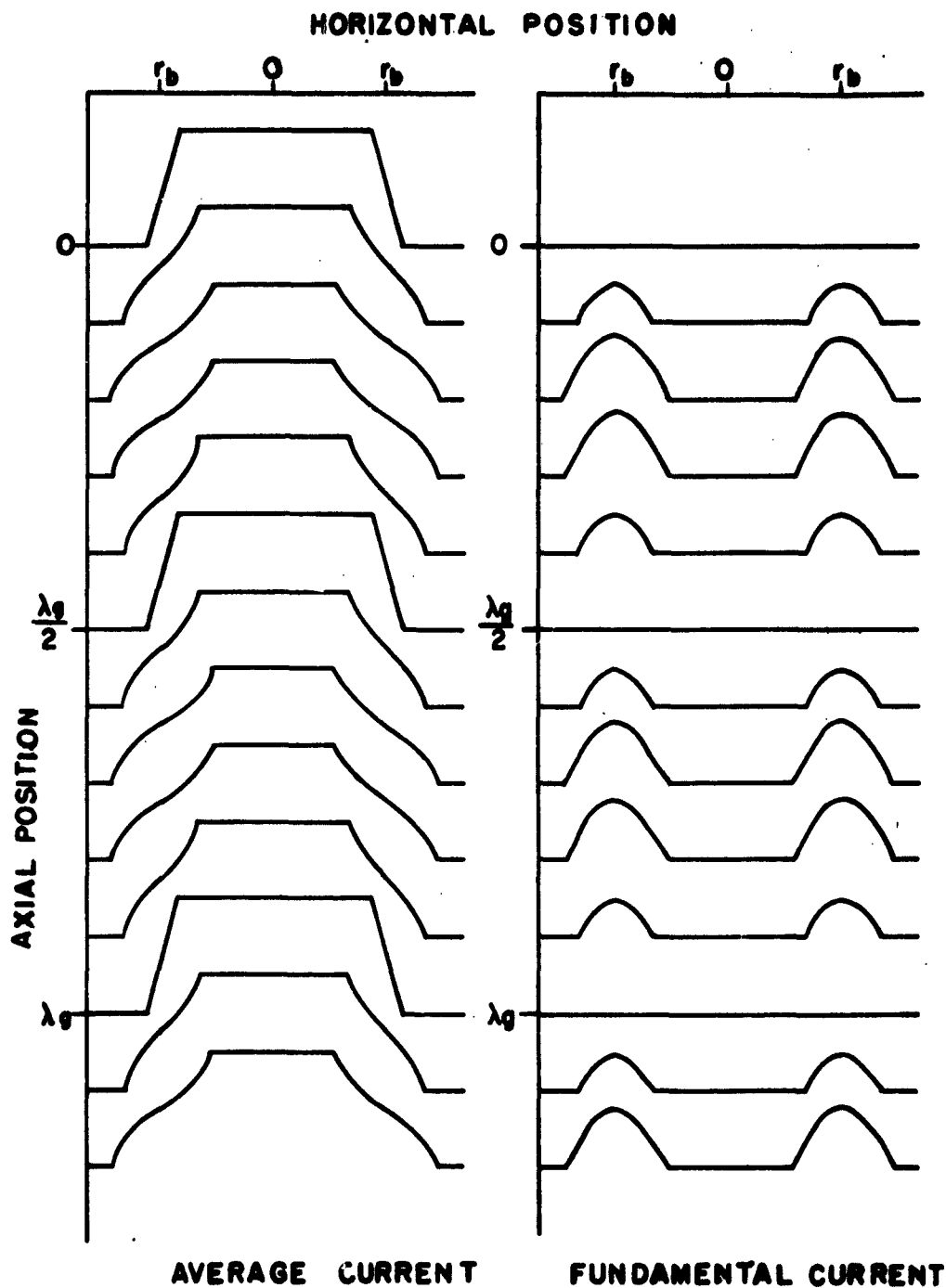


Figure 11. Approximate Current Densities as Functions of Horizontal and Axial Positions in Trapezoidal Beam.

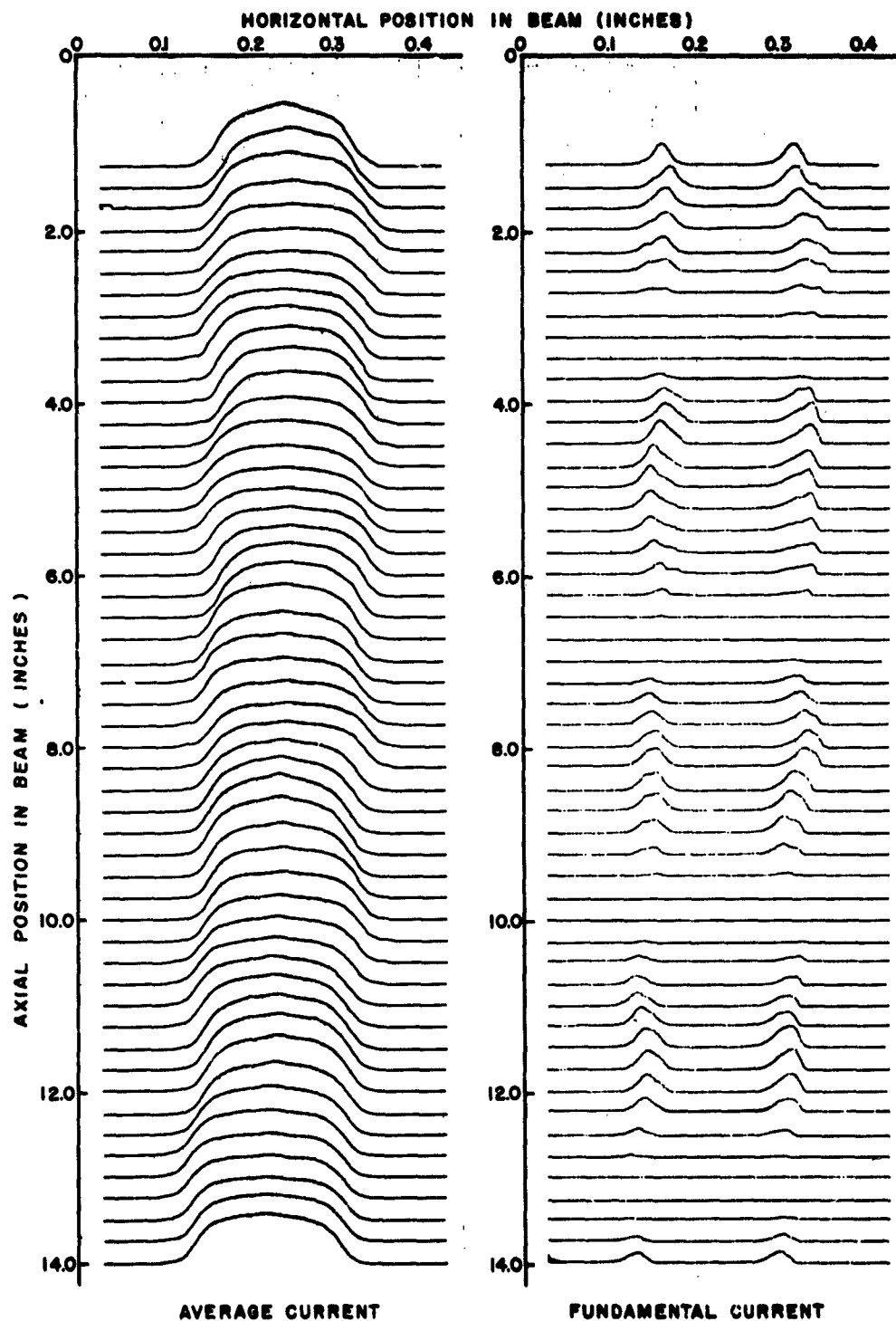


Figure 12. Average and Fundamental Current-Density Plots as Functions of Horizontal and Axial Positions in Beam for an  $\alpha$  of .041.

profiles and the profiles of the d-c Brillouin beam are not apparent. Except for irregularities caused for higher-order effects at the edge of the d-c beam, the fundamental current pattern is very much like that shown in Figure 11. Notice that both the width and the amplitude of the current peaks vary with distance. This same effect has been reported by Winslow.<sup>9</sup> Unfortunately, no calibration of the r-f current probe was possible, so that the amplitudes of the fundamental current curves must not be compared with the amplitudes of the average current curves in Figure 12 or in succeeding figures in this report.

Shown in Figure 13 are plots of the peak velocity of the beam as a function of axial position for the  $\alpha$  of .041 of Figure 12 as well as for several other values of  $\alpha$ . For the two lowest values of  $\alpha$ , these curves are seen to be nearly as predicted by theory. The main deviations have been pointed out in the literature<sup>3</sup> and are: (1) that the nulls do not reach the d-c beam level, and (2) that the maxima decrease slightly with distance. A possible explanation of this behavior is given in an earlier paper.<sup>3</sup> It should be mentioned here that the experimental value of the plasma-frequency reduction factor determined on the basis of data given in Figures 12 and 13, as well as in an earlier study,<sup>3</sup> is 0.42. This agrees extremely well with the value of 0.413 obtained from Equation (34) in Figure 4.

Shown in Figure 14 are plots of the average and fundamental currents; these, however, are for  $\alpha = .083$ . Notice that both the amplitudes and the widths of the fundamental current peaks are greater than those given in Figure 12. No harmonic data are available at the drive levels of Figure 12 and 14 because the harmonic currents were found to be partially or totally masked by the noise of the receiver system used for current measurements.

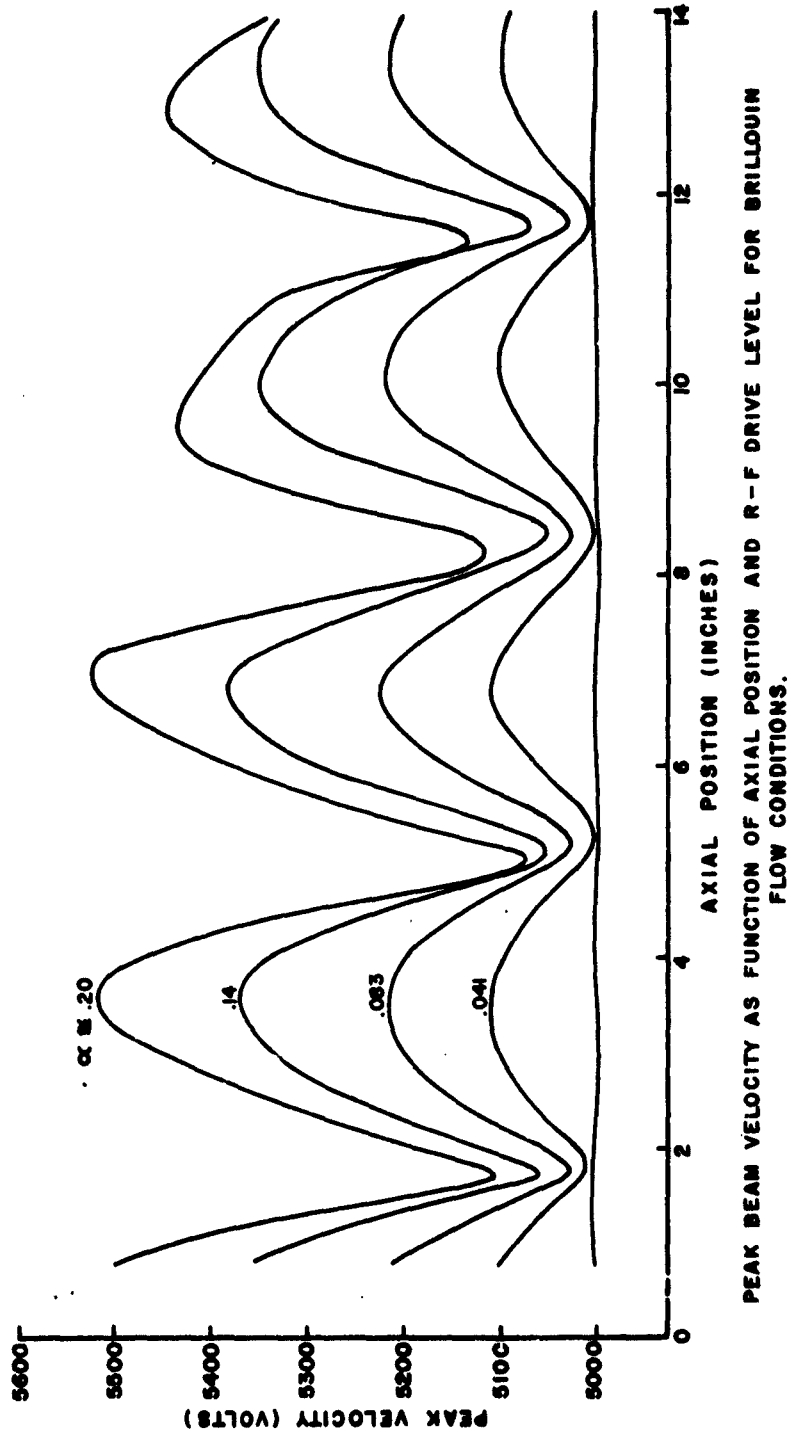


Figure 13. Peak Beam Velocity as Function of Axial Position and R-F Drive Level for Brillouin Flow Conditions.



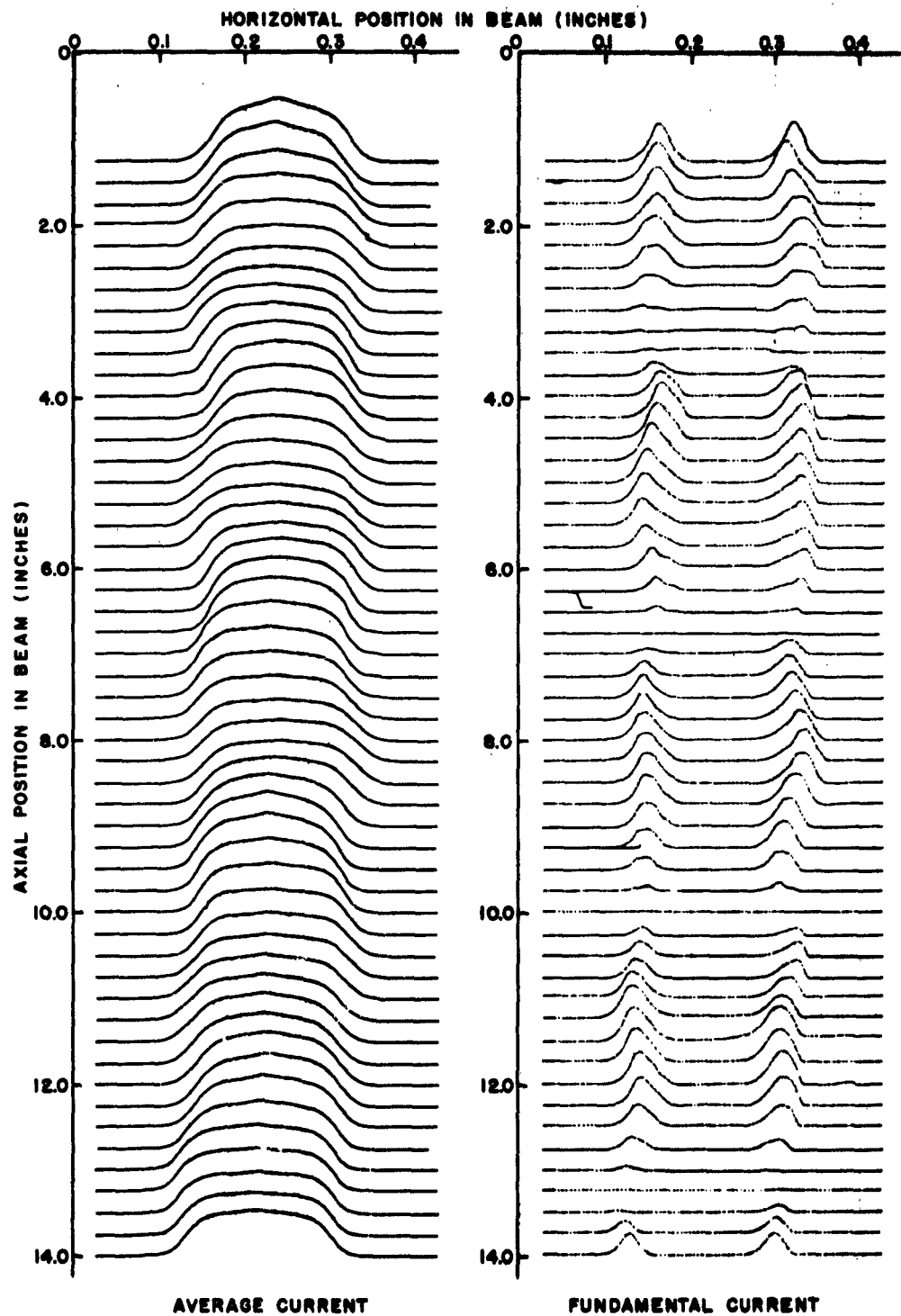


Figure 14. Average and Fundamental Current-Density Plots as Functions of Horizontal and Axial Positions in Beam for an  $\alpha$  of .083.

### III. BRILLOUIN BEAM WITH LARGE-SIGNAL MODULATION

Although considerable effort has been devoted to the large-signal analysis of Brillouin beams, a satisfactory theory has not yet been formulated; therefore, this section contains experimental results of large-signal Brillouin beam and a qualitative rather than quantitative discussion of the results.

Shown in Figures 15 and 16 are curves of the average and fundamental currents for values of  $\alpha$  of 0.14 and 0.20. The  $\alpha = 0.14$  curves show that the amplitudes and widths of the fundamental current peaks have increased when  $\alpha$  was increased. The curves of  $\alpha = 0.20$ , however, show a further increase in the width of the current peaks, but, little or no increase in the amplitude of peaks. Thus the development shown in Figure 10 for large values of  $\alpha$  has been reached.

Spreading of the average current profiles where maxima in the fundamental current profiles occur is evident in Figures 15 and 16. These average current profiles are similar to those predicted in Figure 11. The main differences are due to the d-c beam profile not being quite trapezoidal but having rounded corners instead. This means, of course, that the average current profiles should not have the sharp corners shown in Figure 11. One important nonlinear effect that is most easily noticeable in Figure 16 is the narrowing of the average current profiles to diameters smaller than the d-c Brillouin beam diameter. Because of the enlarged radial motions near the surface, an average nonlinear force arises, which is directed radially inward. This causes a sharp beam focus one-quarter of a reduced plasma wavelength from the fundamental current maxima. For drives as large and

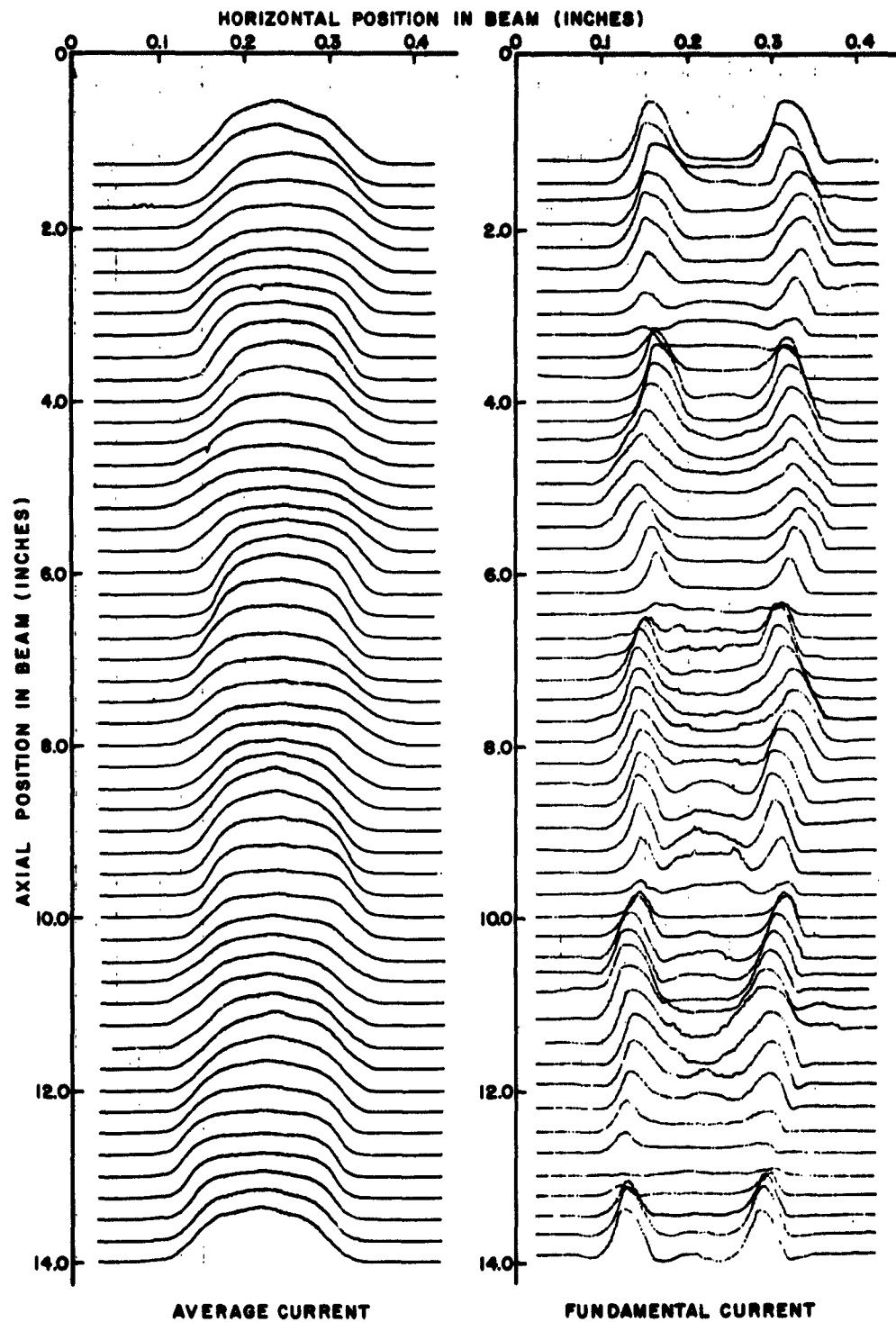


Figure 15. Average and Fundamental Current-Density Plots as Functions of Horizontal and Axial Positions in Beam for an  $\alpha$  of 0.14.

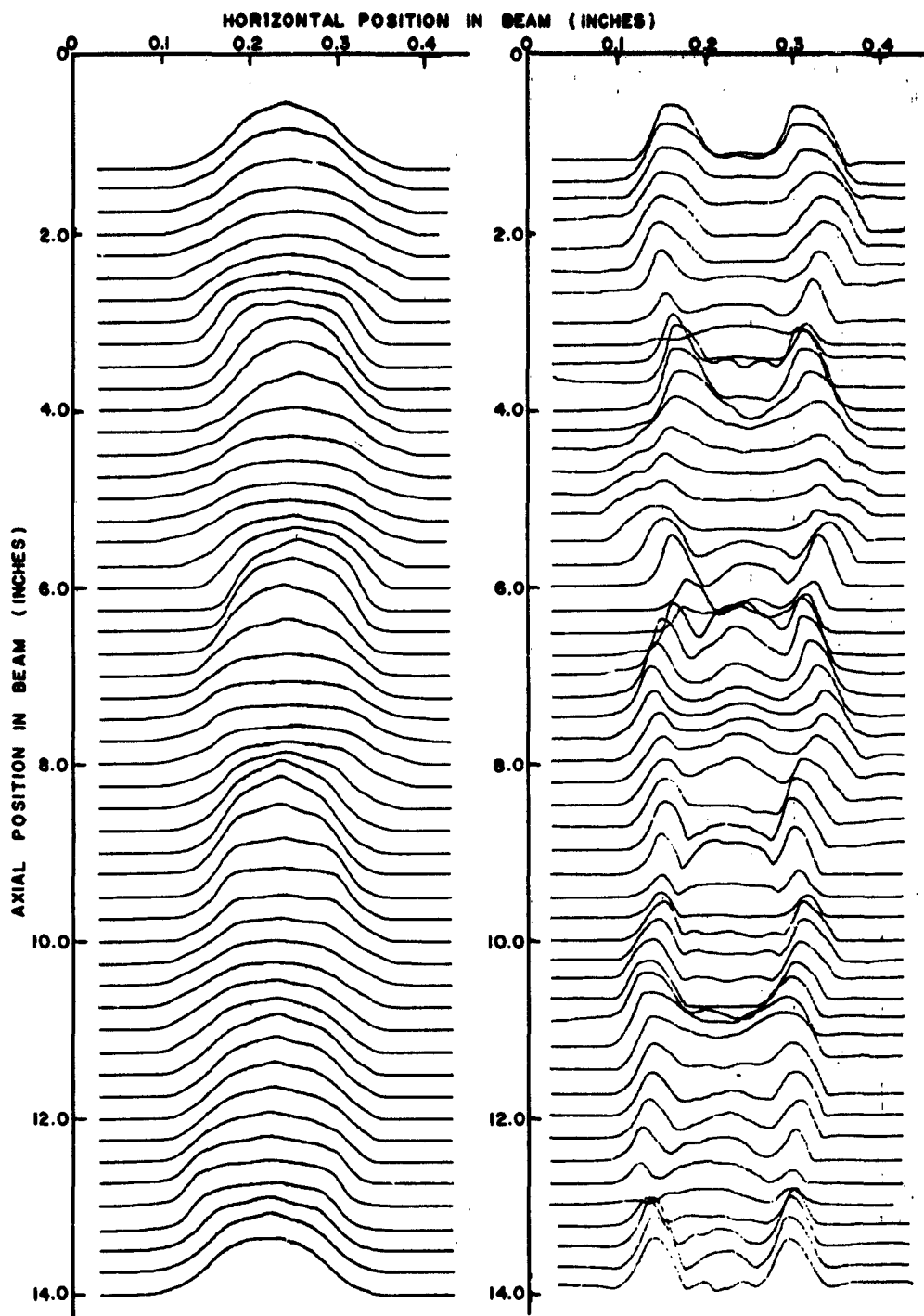


Figure 16. Average and Fundamental Current-Density Plots as Functions of Horizontal and Axial Positions in Beam for an  $\alpha$  of 0.20.

larger than the one used in Figure 16, the average current density at the beam center is altered, and severe alteration of beam spreading and beam focusing are noticeable with distance. This is especially evident in Figure 16 after the second null in the surface current.

It may be noticed that a small amount of volumetric fundamental current density has arisen in Figures 15 and 16, especially at larger drift distances. A portion of this current density is clearly the  $\rho_0 \frac{1}{2}$  component, which is predicted by the small-signal Brillouin beam theory. A second portion of this current density arises from nonlinear effects and is relatively irregular and never large when reasonable wave-like behavior is observed.

Second-harmonic current-density profiles for drive levels of  $a = .14$  and  $a = .20$  are shown in Figure 17. These are considerably lower in amplitude than the fundamental current densities for the same drive levels and remain mainly as surface currents. Since no calibration of the circuit for the second-harmonic current was possible when the second harmonic data was taken, no comparison of absolute amplitudes of fundamental and second-harmonic currents is possible. There appear to be at least two current waves present in the data shown in Figure 17. The first is the component arising from the square-wave current-density wave at the edges of the beam. This component was predicted in Section II. A second component is present, which is thought to have arisen from a wave at the second-harmonic frequency launched at the cavity by the nonlinear drive in the high alternating fields in the gap. This wave has its own standing-wave period along the beam, which is considerably less than that for the fundamental frequency because of a larger plasma-frequency reduction factor at the

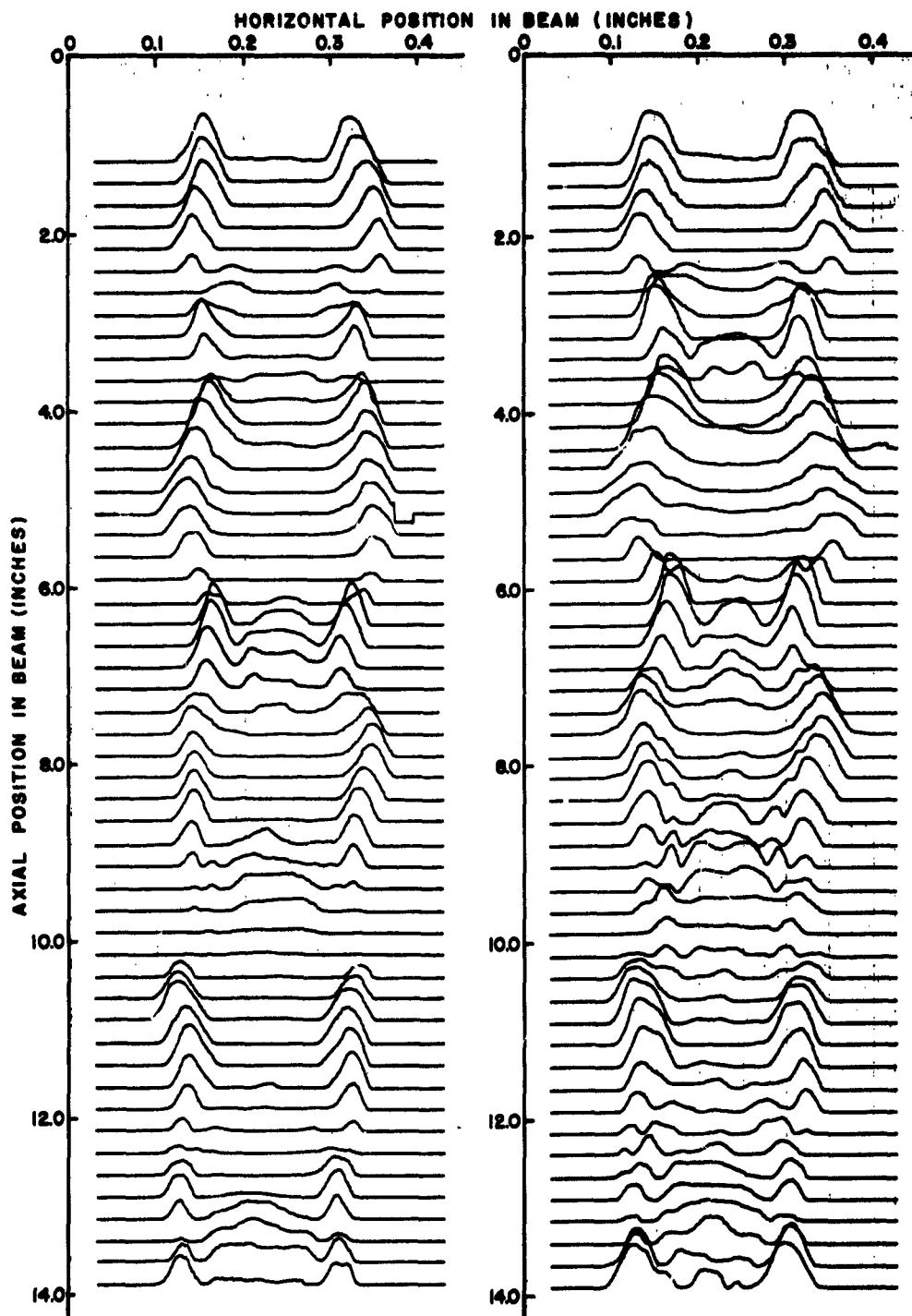


Figure 17. Second-Harmonic Current-Density Plots as Functions of Horizontal and Axial Positions in Beam for  $\alpha = .14$  (left) and  $\alpha = .20$  (right).

second-harmonic frequency. The ratio of the second-harmonic to the fundamental frequency-reduction factor determined from Figures 17 and 13 is approximately 1.27 and that obtained from Figure 4 is 1.33, which supports the idea that a second-harmonic signal is launched by the cavity.

It can be seen that when this short-period component with a single maximum in radius goes to zero, the long-period component with its double maximum in radius remains. Note also that the longitudinally spaced zeros of the second-harmonic current density are less regular than those of the fundamental current density. This is due to the two waves with different reduced plasma wavelengths beating with each other with distance.

Third-harmonic current-density contours across the beam as a function of drift distance for the drive level  $\alpha = .14$  are shown in Figure 18. As in the second harmonic case, the current is predominantly at the surface and is quite small, no comparison of absolute amplitudes can be made, and a component launched by the nonlinear field in the gap is present but now the magnitude of this component is not too much larger than the component resulting from large alternating positions at the fundamental frequency. The component caused by the nonlinear field has an even shorter period than that of the second harmonic, because it is a third-harmonic wave, having a still larger plasma-frequency reduction factor than the second-harmonic wave. In this case, the experimental ratio of the reduction factor of the third harmonic to fundamental frequency is about 1.53, and the predicted ratio is 1.47, indicating very good agreement. The irregular longitudinal spacings of the zeros is present as in the second harmonic, but is complicated by a small, comparable, body current density.

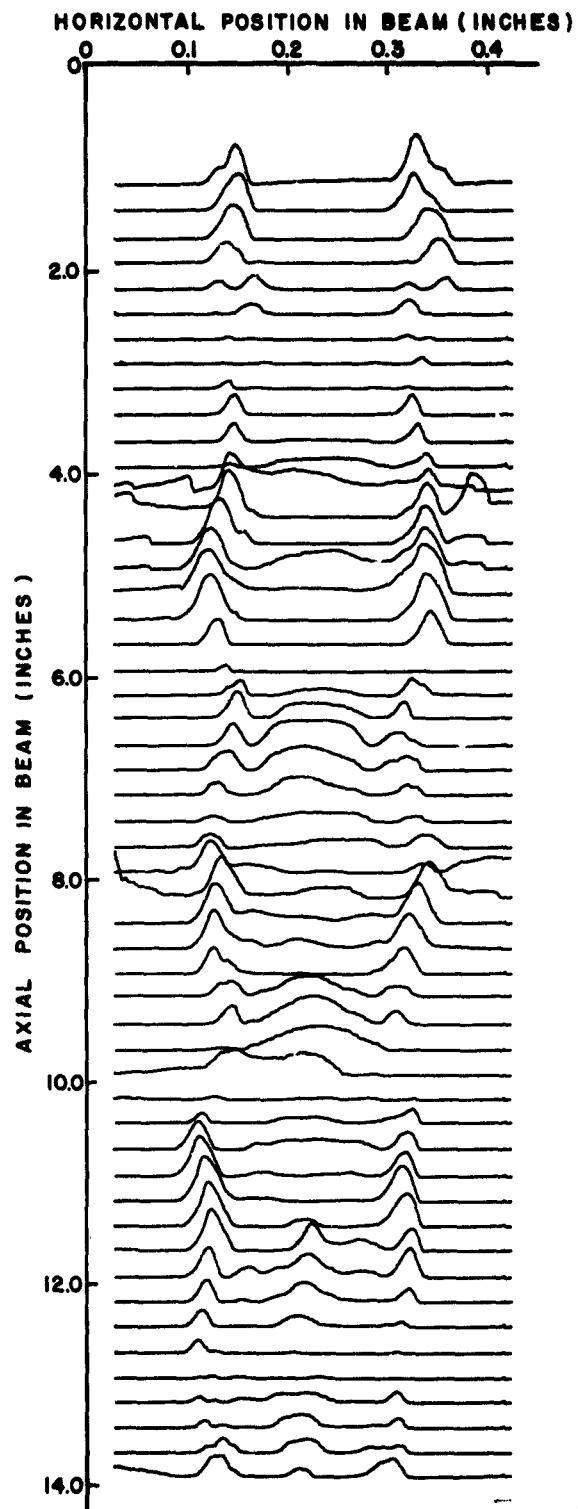


Figure 18. Third-Harmonic Current-Density Plots as Functions of Horizontal and Axial Positions in Beam for  $\alpha = .14$ .



#### IV. CONCLUSIONS AND RECOMMENDATIONS

In conclusion, it may be said that the small-signal theory of the Brillouin beam accurately describes the r-f forces in the beam because (1) the r-f current-density profiles determined experimentally display the shell of surface current predicted by the theory and (2) the measured plasma-frequency reduction factor is nearly identical to the predicted value. In addition, it appears that the modification made in the theory for beams with trapezoidal cross sections is valid, since the shapes of the experimental r-f current contours agree well with those predicted by theory.

From the discussion of the large-signal effects, it is apparent that the nonlinear forces arising in the beam are not well understood, and it is recommended that continued efforts be devoted to the formulation of a satisfactory nonlinear theory.

## APPENDIX: PROBE CIRCUITRY FOR MEASURING R-F CURRENT

The beam analyzer used in obtaining the r-f current data presented in this report is the one described by Gilmour<sup>1,3</sup> and Hallock<sup>2</sup>. The important features of this analyzer, and the r-f current-measuring probe and circuitry, are described here. The parts of the analyzer essential to the r-f current measurements are shown in Figure A-1. The electron beam, on which measurements were made, was generated by the shielded Pierce gun shown at the right side of the figure. This gun was normally pulse operated at 5000 volts and had a microperveance of 1.15. The area compression of the beam was 50:1, and the magnetic field required for Brillouin flow (less than 2 per cent scalloping) was 285 gauss.

As is shown in Figure A-1, a ball valve was positioned between the gun and the drift region which contained a doubly re-entrant cavity and a beam-analyzing mechanism. This valve is considered to be one of the most important parts of the analyzer because when it is closed, the drift tube can be opened to atmospheric pressure while the cathode remains in a region evacuated to a pressure of about  $10^{-9}$  mm Hg. When the drift tube is evacuated, the valve is opened and the beam from the gun passes through the aperture in the ball to the beam-modulating and beam-analyzing region.

### A. PROBE

The beam-analyzing mechanism shown at the left of Figure A-1 is shown again in Figure A-2 and also in the photograph in Figure A-3. Most of the electron beam was collected by the beam-collecting plate, which was carbonized to reduce the secondary electron ratio. A small portion, however,

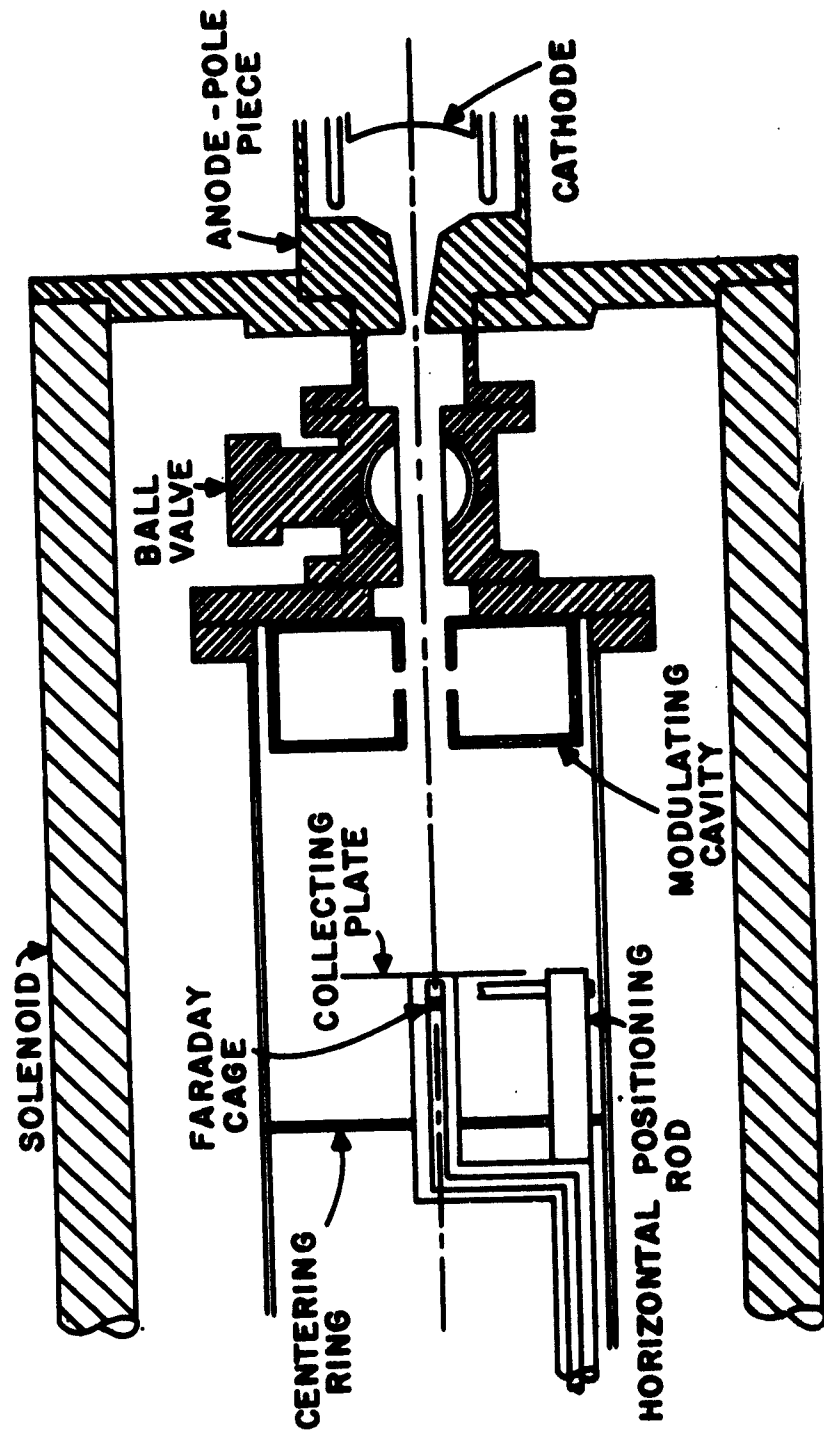


Figure A-1. Simplified Sketch of Beam Analyzer.

was allowed to pass through the 0.010-inch aperture in the center of the plate to a Faraday cage. The Faraday cage, in turn, was attached to the end of the center conductor of a nonresonant coaxial line, which proved to be valuable in measuring currents at frequencies from d-c to 6000 Mc/s. Since the distance between the Faraday cage and the beam-collecting plate was about 0.030 inch, the electron transit angle between the plate and the cage was less than 0.25 radians under normal operating conditions. The gap-coupling coefficient for the current under these conditions was unity, for all practical purposes, and that for velocity was zero. As is shown in Figure A-2b, a short portion of the coaxial line directly behind the beam-collecting plate was flexible, so that the plate could be moved with respect to the fixed part of the coaxial line. The reason for moving the plate was, of course, to make beam measurements at any point in a plane perpendicular to the axis of the beam.

The electron current from the cage went out through a coaxial feed-through in the bottom control rod to an indicating device outside the analyzer. The collecting plate was positioned in the plane perpendicular to the axis of the solenoid by rotations of the two control rods. As is shown in Figure A-2b, the plate could be moved horizontally by rotating the bottom rod. Vertical motion was produced in a similar manner by rotating the side rod. Teflon bearings, which were used to prevent binding between stainless steel parts, were attached to the back of the plate and slid on the lever arms attached to the side and bottom rods during horizontal and vertical motion. Although rotational motions were converted to translational motions in positioning the cage, they could be considered to be linear, since the distances moved were small compared to the length of the lever arms.

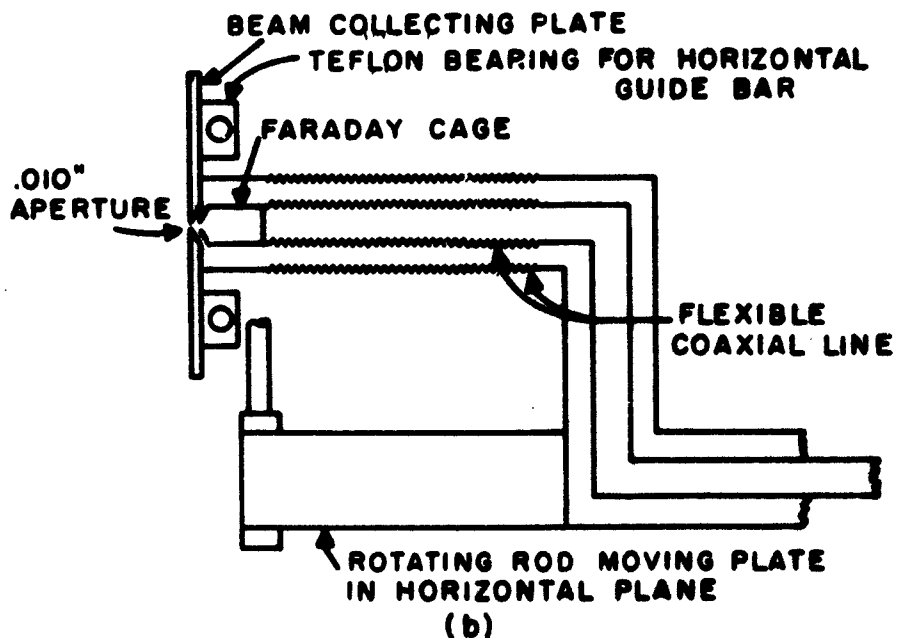
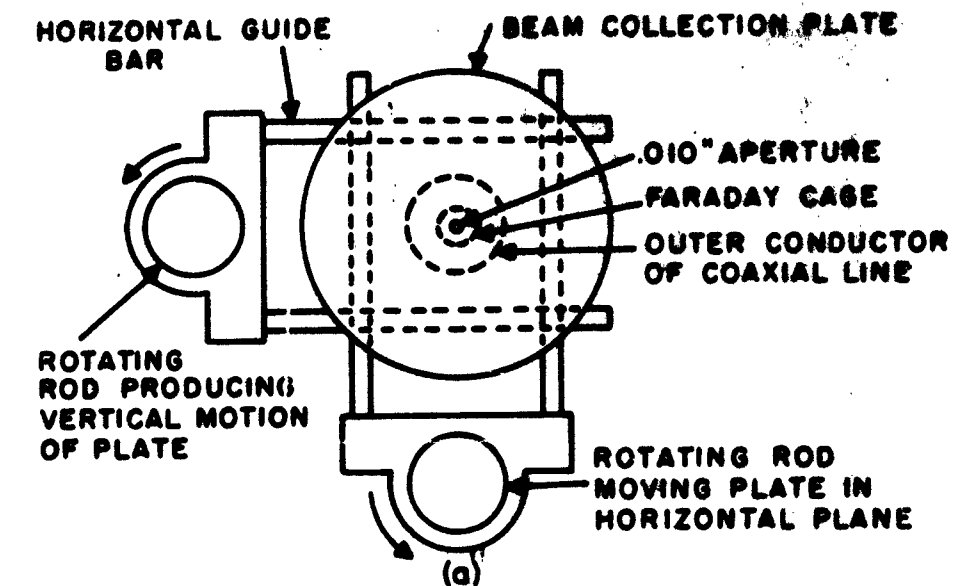
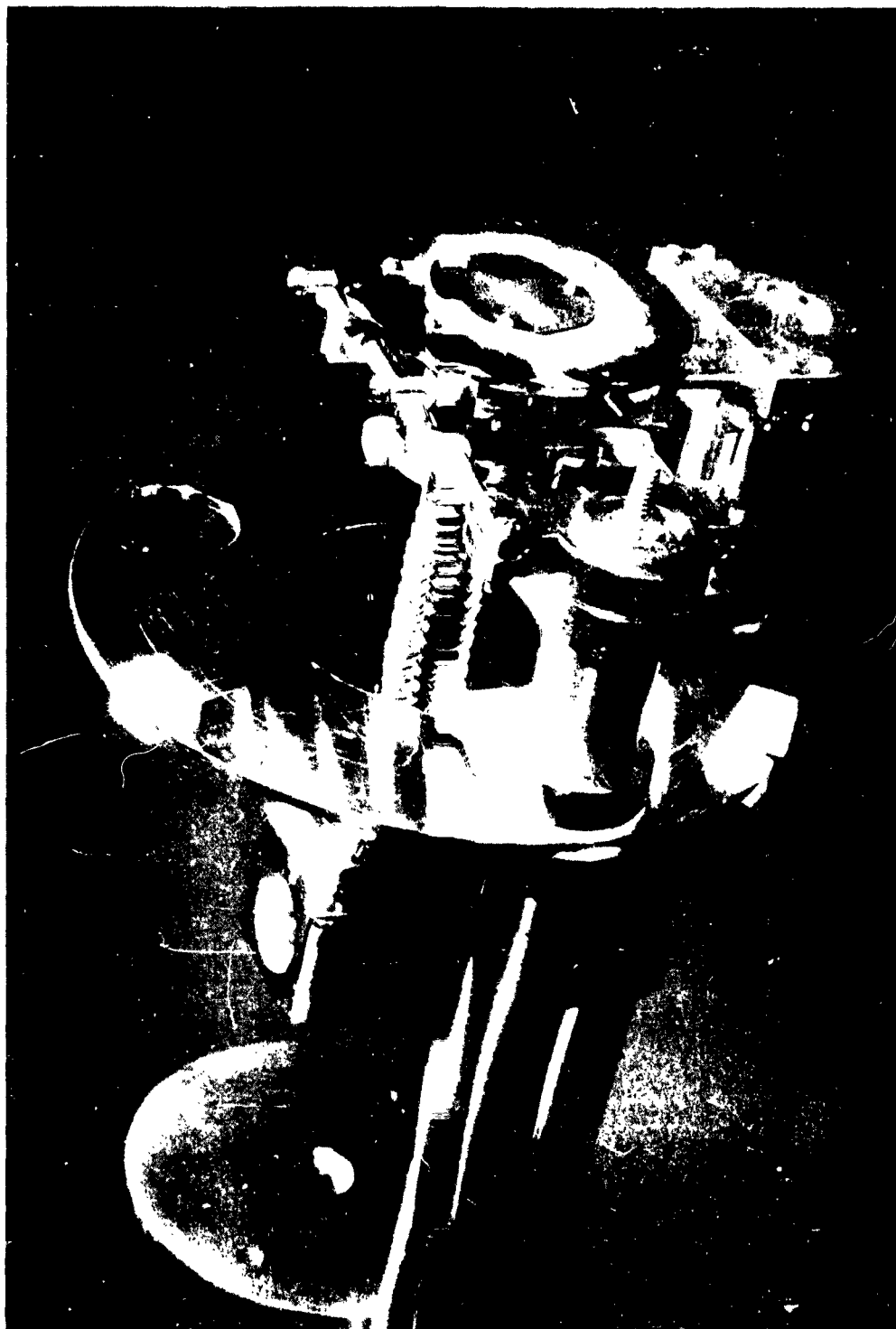


Figure A-2. (a) Simplified Sketch of Beam Scanner. (b) Simplified Sketch of Faraday Cage and Flexible Coaxial Line.



The collecting plate and positioning rods are illustrated in Figure A-3. The disk shown behind the collecting plate and the lever arms was used to center the entire mechanism in the drift tube. Axial motion of the cage assembly was produced by moving the control rods through Veeco quick couplings.

Figure A-4 shows the control mechanism for the positioning rods. The scanning mechanism was moved axially by using the gear and rack arrangement shown in the figure. The angular position of the rods was adjusted by means of micrometers, the micrometer that set the horizontal position of the Faraday cage being equipped with a motor drive. Reversing switches caused the motor to sweep the cage back and forth across the beam automatically. To provide a voltage proportioned to the horizontal position of the cage, a ten-turn helipot was geared to the motor. This voltage was applied to the X input of an X-Y recorder and a voltage proportional to the r-f current component selected by the Faraday cage circuit was applied to the Y input of the X-Y recorder so that automatic plotting of current amplitudes as a function of position in the beam was possible.

## B. CIRCUITRY

A block diagram of the circuit used for measuring the r-f currents received by the Faraday cage is shown in Figure A-5. The modulated beam was sampled by the beam-collecting plate with a .010-inch aperture in the center. The current passing through the aperture was collected by the Faraday cage and was taken out of the analyzer through the nonresonant coaxial line. At this point, a filter was used to select the harmonic to be analyzed. After the filtering process, a path was provided for d-c current to return

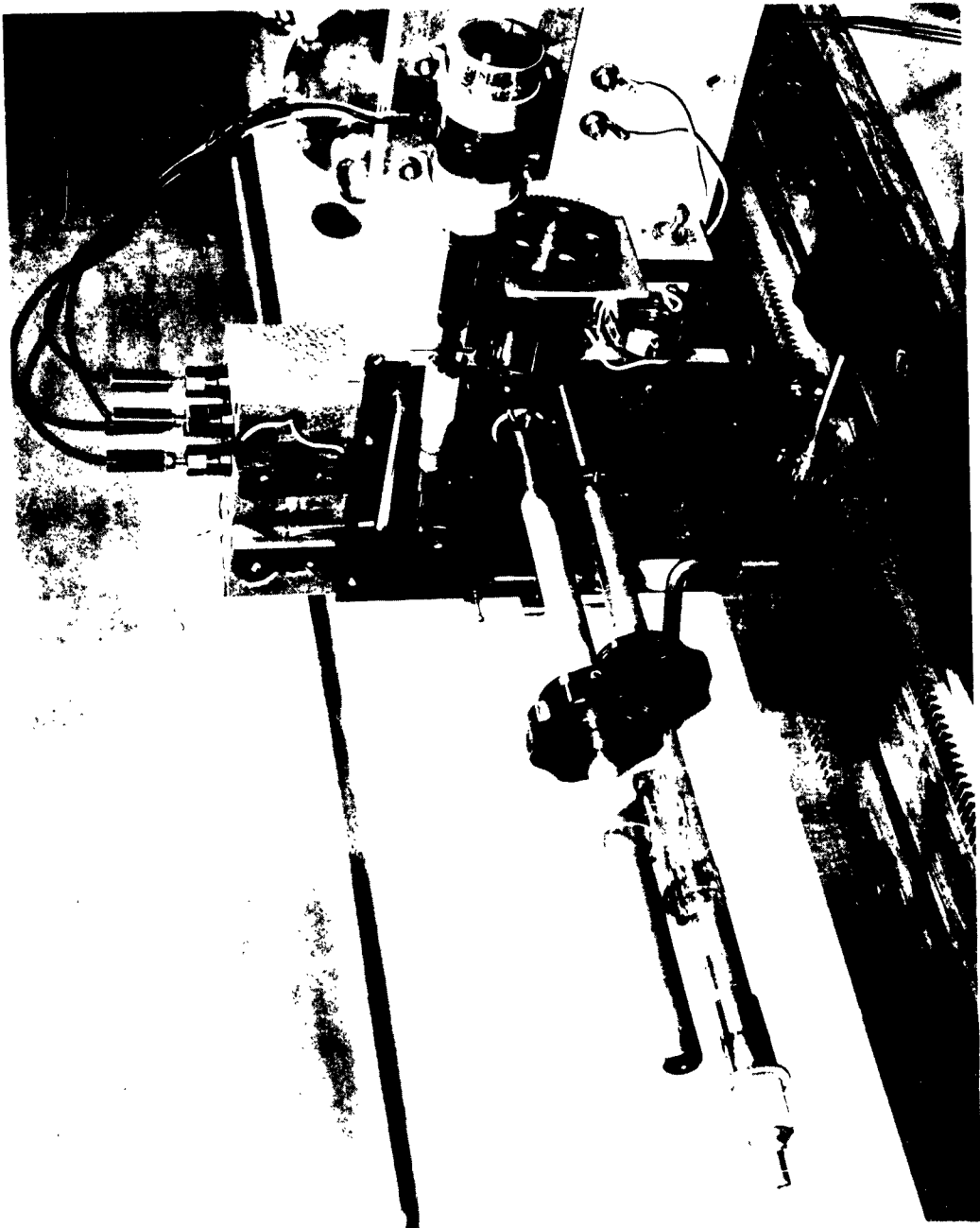


Figure A-4 Control-Rod Positioning Mechanism.



to ground, and in fact, a recorder was normally included in this circuit when measurements were being made of the fundamental r-f current component, so that the shape of the average-current profile in the beam could be obtained simultaneously. Following the d-c current connection, a capacitor was inserted in the line to eliminate parallel d-c current paths, and a variable impedance was inserted to optimize the r-f signal amplitudes arriving at the crystal mixer.

A local oscillator is shown in the lower left-hand corner of Figure A-5 and was used to obtain a 30-Mc/s intermediate frequency from the crystal mixer. A filter and an isolator were used in the local-oscillator circuit to prevent interference from local-oscillator harmonics and to isolate the local oscillator from impedance changes occurring in the r-f current-sensing circuit.

A General Radio Type 1216-A unit i-f amplifier was used to amplify the 30 Mc/s intermediate frequency generated by the crystal mixer. Since the output voltage from the i-f amplifier was not directly proportional to the amplitude of the 30 Mc/s signal fed into the amplifier, a nonlinear circuit was devised, which compensated for the nonlinearities in the i-f amplifier. The amplitude of the output pulse from this linearizing circuit was therefore proportional to the amplitude of the 30 Mc/s signal and also proportional to the r-f current signal from the beam, since the crystal mixer was operated in a linear range.

Finally, the pulse from the linearizing circuit was amplified and fed into a circuit which generated a d-c voltage equal to the peak pulse voltage. This d-c voltage, which was then proportional to the r-f current signal from the beam, was amplified by a General Radio Type 1230-A d-c ampli-

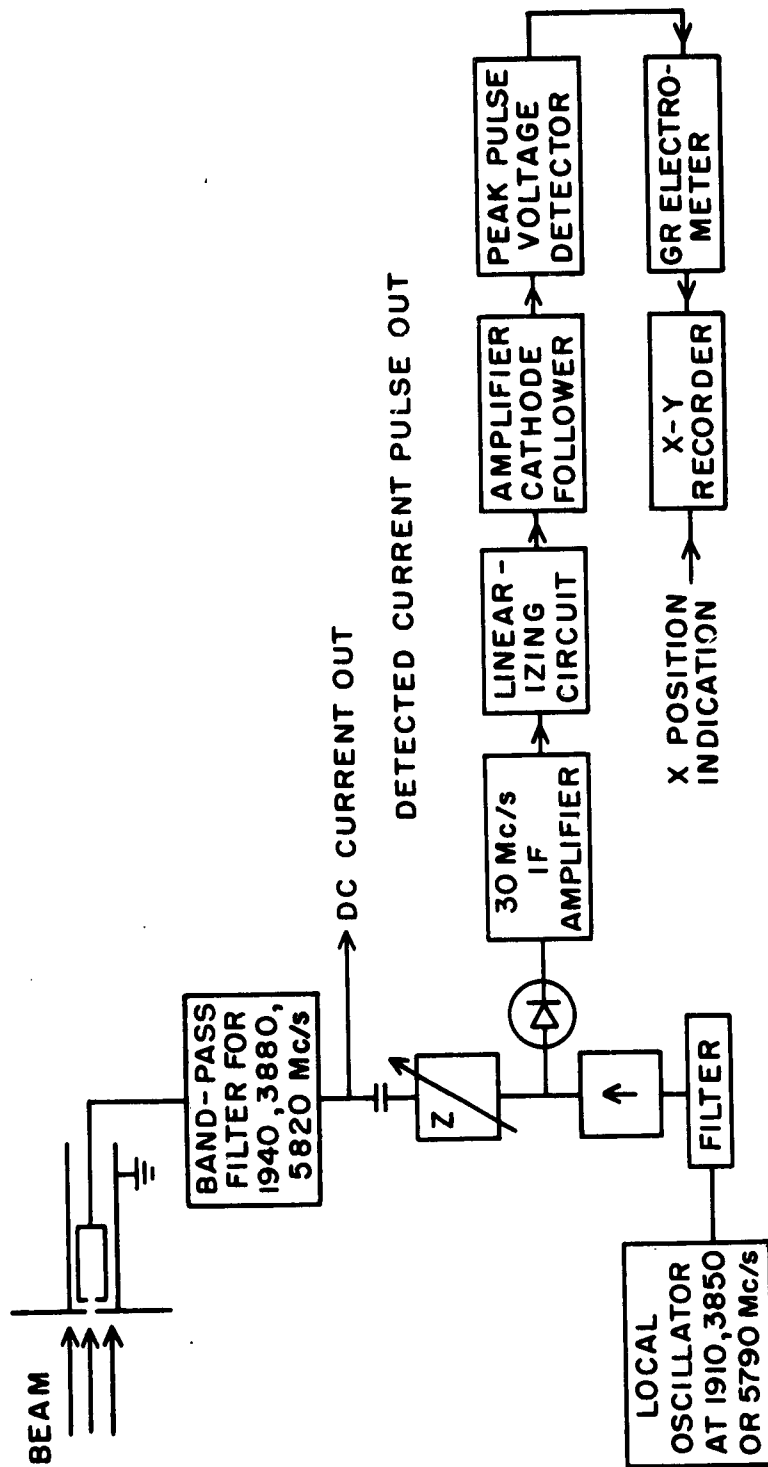


Figure A-5. Circuit Used in Detecting and Recording R-F Currents in Modulated Electron Beam.

fier and was applied to the Y input of an X-Y recorder. The voltage applied to the X input of the recorder was, as usual, proportional to the X position of the Faraday cage in the electron beam. As a result, by using the circuit shown in Figure A-5, the amplitude of the r-f current density in the beam could be recorded directly as a function of position in the beam.

# GRAPHIC SYMBOLS FOR MICROWAVE SCHEMATIC DIAGRAMS

<u>ATTENUATORS</u>	<u>CAVITIES</u>	<u>COUPLERS</u>	<u>DETECTORS</u>	<u>ELECTRONIC EQUIPMENT</u>	<u>FILTERS</u>
 FIXED 3DB	 SINGLE PORT	 CROSS GUIDE 20 DB	 CRYSTAL & MOUNT	 POWER BRIDGE	 2 KMc LOW PASS
 ADJUSTABLE	 DOUBLE PORT	 H ARM "T"	 BOLMETER & MOUNT	 I.F. AMPLIFIER	 2 KMc HIGH PASS
 ADJUSTABLE 10DB MAX.	 DOUBLE PORT ADJUSTABLE	 MAGIC "T"	 THERMISTOR & MOUNT	 OSCILLOSCOPE (Y AXIS)	 2-4 KMc BAND PASS
 WAVE GUIDE BEYOND CUTOFF				 POWER SUPPLY WITH BUILT IN 1000 CYCLE SQUARE WAVE MODULATION	
<u>IMPEDANCE TRANSFORMERS</u>	<u>TERMINATIONS</u>	<u>TUBES</u>	<u>WAVE METERS</u>	<u>MISCELLANEOUS</u>	
 FIXED	 FIXED MATCHED LOAD	 KLYSTRON OSCILLATOR WITH 1000 CYCLE SQUARE WAVE MODULATION	 TRANSMISSION	 PHASE SHIFTER	
 ADJUSTABLE	 ADJUSTABLE LOAD	 BACKWARD WAVE OSCILLATOR WITH NO MODULATION	 REACTION	 LOCAL OSCILLATOR (WHERE TYPE IS UNIMPORTANT)	
	 SLIDING SHORT CIRCUIT	 2-CAVITY KLYSTRON AMPLIFIER		 ISOLATOR	
		 TRAVELING WAVE TUBE		 SLOTTED LINES	
		 MULTICAVITY KLYSTRON AMPLIFIER		 OSCILLATOR WITH 1000 CYCLE SQUARE WAVE MODULATION (WHERE TYPE IS UNIMPORTANT)	

## REFERENCES

1. A. S. Gilmour, Jr., "A Beam Tester for Studying the Characteristics of D-C and Velocity-modulated Electron Beams," Research Report EE 495, Cornell University, 1961.
2. D. D. Hallock, "Investigation on the Laminarity of Flow in a Magnetically Confined Electron Beam," Research Report EE 539, Cornell University, 1962.
3. A. S. Gilmour, Jr., "The Velocity Distribution in a Velocity-modulated Electron Beam from a Shielded Pierce Gun," Research Report EE 507, Cornell University, 1961.
4. W. W. Rigrod and J. A. Lewis, "Wave Propagation along a Magnetically Focused Cylindrical Electron Beam," Bell Sys. Tech. Jour., 33 (1954), pp. 399-416.
5. L. Brillouin, "A Theorem of Larmor and its Importance for Electrons in Magnetic Fields," Phys. Rev., 67 (1945), p. 260.
6. A. L. Samuel, "On the Theory of Axially Symmetric Electron Beams in an Axial Magnetic Field," Proc. I.R.E., 37 (1949), p. 1252.
7. C. C. Wang, "Electron Beams in Axially Symmetrical Electric and Magnetic Fields," Proc. I.R.E., 38 (1950), pp. 135-147.
8. M. Chodorow and L. T. Zitelli, "The Radio-Frequency Current Distribution in Brillouin Flow," I.R.E. Trans., ED-6 (1959), pp. 352-357.
9. D. K. Winslow, "The Current Distribution in Magnetically Focused Modulated Electron Beams," Rep. No. 380, Stanford Univ., Microwave Laboratory, Stanford, Cal., April 1957.